Title

Single-Cell Profiles of Retinal Ganglion Cells Differing in Resilience to Injury Reveal Neuroprotective Genes

Journal

Neuron, 104(6)

ISSN

0896-6273

Authors

Tran, Nicholas M
Shekhar, Karthik
Whitney, Irene E
et al.

Publication Date

2019-12-01

DOI

10.1016/j.neuron.2019.11.006

Published in final edited form as:

Neuron. 2019 December 18; 104(6): 1039–1055.e12. doi:10.1016/j.neuron.2019.11.006.

Single-cell profiles of retinal ganglion cells differing in resilience to injury reveal neuroprotective genes

Nicholas M. Tran[1,7], **Karthik Shekhar**[2,7], **Irene E. Whitney**[1,7], **Anne Jacobi**[3,7], **Inbal Benhar**[2,8], **Guosong Hong**[4,5,8], **Wenjun Yan**[1], **Xian Adiconis**[2], **McKinzie E. Arnold**[3], **Jung Min Lee**[4], **Joshua Z. Levin**[2], **Dingchang Lin**[4], **Chen Wang**[3], **Charles M. Lieber**[4], **Aviv Regev**[2,6], **Zhigang He**[3], **Joshua R. Sanes**[1,+]

[1]Center for Brain Science and Department of Molecular and Cellular Biology, Harvard

[2]Broad Institute of Harvard and MIT, Cambridge, MA 02142

[3]F.M. Kirby Neurobiology Center, Department of Neurology, Boston Children's Hospital, Harvard Medical School, Boston, MA 02115

[4]Department of Chemistry and Chemical Biology, Harvard University, Cambridge, MA 02138

[5]Department of Material Science and Engineering and Wu Tsai Neurosciences Institute, Stanford University, CA 94305

[6]Howard Hughes Medical Institute, Chevy Chase, MD 20815, USA and Department of Biology and Koch Institute, MIT, Cambridge, MA 02139

[7]These authors contributed equally

[8]These authors contributed equally

SUMMARY

Neuronal types in the central nervous system differ dramatically in their resilience to injury or insults. Here we studied the selective resilience of mouse retinal ganglion cells (RGCs) following optic nerve crush (ONC), which severs their axons and leads to death of ~80% of RGCs within 2 weeks. To identify expression programs associated with differential resilience, we first used single-cell RNA-seq (scRNA-seq) to generate a comprehensive molecular atlas of 46 RGC types in adult retina. We then tracked their survival after ONC, characterized transcriptomic, physiological, and morphological changes that preceded degeneration, and identified genes

[+]Lead Contact: sanesj@mcb.harvard.edu.

AUTHOR CONTRIBUTIONS

N.M.T., K.S., I.E.W., A.J., I.B., G.H., and J.R.S. conceived and designed experiments and analyzed data. N.M.T., I.E.W., A.J., I.B., G.H., W.C and M.E.A. performed experiments. K. S. developed the computational approaches. X.A. and J.Z.L. generated Smart-seq2 libraries. J.M.L and D.L. assisted with in vivo recordings. W.Y. analyzed data. C.M.L., A.R., Z.H. and J.R.S. provided supervision and acquired funding. N.M.T., K.S., I.E.W., A.J. and J.R.S. wrote the paper with input from all authors.

DECLARATION OF INTERESTS

AR is an equity holder in Celsius Therapeutics and a SAB member in Syros Pharmaceuticals and Thermo Fisher Scientific. JRS is a consultant for Biogen.

selectively expressed by each type. Finally, using loss- and gain-of-function assays *in vivo*, we showed that manipulating some of these genes improved neuronal survival and axon regeneration following ONC. This study provides a systematic framework for parsing type-specific responses to injury, and demonstrates that differential gene expression can be used to reveal molecular targets for intervention.

Graphical Abstract

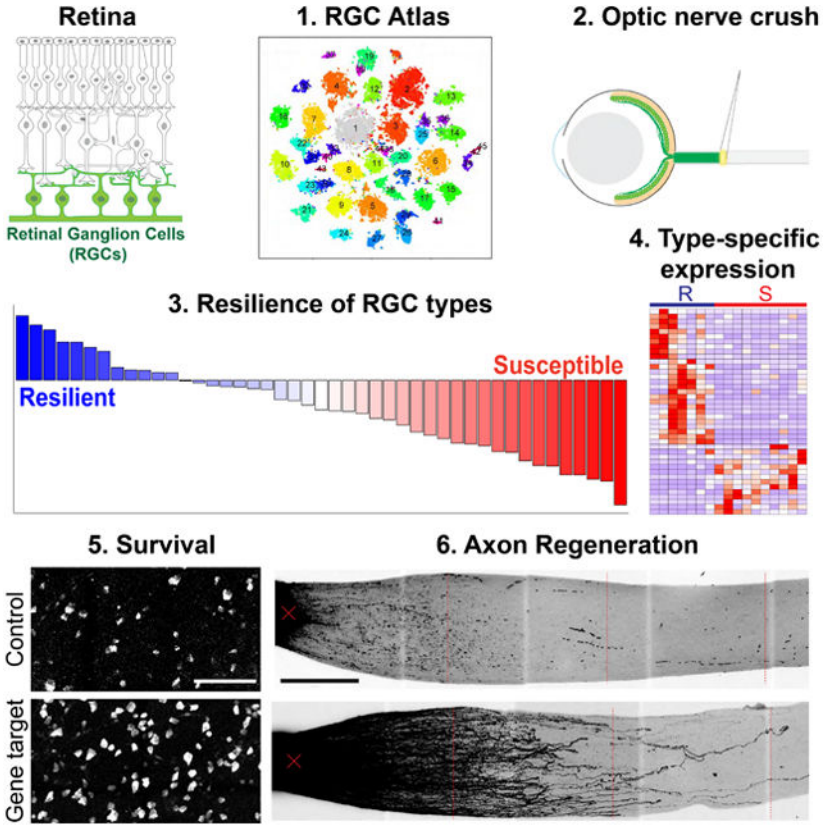

eTOC blurb

High-throughput single cell RNA-seq characterizes 46 types of adult mouse retinal ganglion cells and documents dramatic difference among them in their ability to survive axotomy. Manipulation of genes differentially expressed between resilient and vulnerable types enhances survival and axon regeneration.

INTRODUCTION

Insults to the central nervous system (CNS), whether acute (e.g. traumatic injury) or chronic (e.g. neurodegenerative disease), typically lead to irreversible damage. Some neurons die, and those that survive generally fail to grow new axons and re-establish synaptic connections. A common but poorly understood characteristic of these phenomena is that specific neuronal types are disproportionately affected even though causative insults are widely shared. For example, both huntingtin (*HTT*) and alpha-synuclein (*SNCA*) are

broadly expressed in neurons, but mutations in *HTT* lead to Huntington's disease with striatal GABAergic neurons as a main target, while mutations in *SNCA* lead to Parkinson's disease with basal ganglia dopaminergic neurons as a main target (Fu et al., 2018; Saxena and Caroni, 2011). Similar differential effects have been documented for many other diseases and injuries (Conta Steencken et al., 2011; Welin et al., 2008).

We reasoned that comparing patterns of gene expression among neuronal types that are similar in many respects but differ in vulnerability might pinpoint pathways that contribute to resilience. Although seldom used (Duan et al., 2015; Kaplan et al., 2014; Bray et al., 2019), this approach could complement strategies that involve comparing neurons from different ages (regenerative developing vs. nonregenerative adult neurons; Maclaren and Taylor, 1997), regions (regenerative peripheral vs. nonregenerative central neurons; Huebner and Strittmatter, 2009), or species (regenerative fish vs. nonregenerative mouse neurons; Kizil et al., 2012).

To explore this strategy, we analyzed the responses of mouse retinal ganglion cells (RGCs) to optic nerve crush (ONC), a long-studied model of traumatic axonal injury (Aguayo et al., 1991). RGCs send their axons through the optic nerve, conveying visual information to retinorecipient areas in the brain (Figure 1A; Sanes and Masland, 2015). ONC transects RGC axons, causing the death of ~80% of RGCs within 2 weeks. Few survivors regenerate axons, but some can be provoked to do so by a variety of interventions, although none to date have proven capable of restoring useful vision (Benowitz et al., 2017).

Several features make ONC an ideal model to study differential vulnerability: (1) All and only RGC axons pass through the optic nerve, so injury is precisely controlled, simultaneous and specific. (2) RGCs that live and die share the same microenvironment. (3) Although all RGCs share numerous features, they comprise >40 discrete types in mice, each with distinct morphological and physiological features (Figure 1B, and see below). (4) Some RGC types were recently shown to differ in their ability to survive or regenerate axons following ONC (Duan et al., 2015; Norsworthy et al., 2017; Perez de Sevilla Muller et al., 2014).

To survey the resilience of RGC types, we used single-cell RNA-seq (scRNA-seq), which we previously applied to mouse and macaque retina (Macosko et al., 2015; Peng et al., 2019; Shekhar et al., 2016). We first generated an atlas of 46 molecularly distinct types, and used histological approaches to relate transcriptomic clusters to known and novel RGC types. Using this atlas as a foundation, we surveyed resilience at 6 time points after ONC. We determined the kinetics of loss for each RGC type, finding dramatic differences, and assessed physiological and morphological changes that precede death. We then analyzed expression differences among RGC types, identifying genes that correlated with resilience or susceptibility. Finally, we used loss- and gain-of-function methods *in vivo* to test 10 of these genes, identifying some that regulate RGC survival and/or axon regeneration. Taken together, our work provides a comprehensive molecular atlas of adult RGCs, documents changes preceding degeneration, and demonstrates that this approach can be leveraged to identify novel neuroprotective mechanisms.

RESULTS

An atlas of molecularly defined RGC types

To generate a molecular atlas of RGC types, we isolated RGCs from adult (postnatal day [P]56) mice by fluorescence activated cell sorting (FACS), and profiled them by droplet-based scRNA-seq. Computational analysis of 35,699 high-quality single cell transcriptomes revealed 45 molecularly distinct clusters (Figure 1C), one of which was subsequently subdivided (see below), resulting in 46 types. They ranged in frequency from 0.15% to 8.4% (Figure 1D). All clusters expressed pan-RGC markers such as *Slc17a6* (which encodes the transporter VGLUT2), *Rbpms*, and at least one of the three *Pou4* (*Brn3*) transcription factors (Figure 1E). Some clusters could be matched 1:1 to previously characterized types based on differential expression (DE) of a single gene (e.g., *Jam2* for J-RGCs [Kim et al., 2008] and *Mmp17* for N-ooDSGCs [Kay et al., 2011]), but for most, unique identity was conferred only by two-marker combinations (Figure 1F).

Since ~3 hours elapse between enucleation and RNA capture, we considered that clustering could be influenced by post-mortem transcription. To test this possibility, we analyzed ~11,800 RGCs from retinas treated with the transcription blocker actinomycinD (ActD) immediately after enucleation (Hrvatin et al., 2018; Wu et al., 2017). Although some differences were observed, such as the expected upregulation of immediate early genes (IEGs) in untreated retinas, the frequency of types, and their distinguishing markers were identical between Act-treated and untreated RGCs (Figures 1G,H and S1A,B).

Clusters were reproducible across biological replicates and computational approaches (Figure S1C–F). In addition, we compared the relative frequencies of RGC groups labeled immunohistochemically (IHC) in retinal whole mounts to their frequencies in the scRNA-seq data and found a striking correspondence (Figure 1I). Together, these results indicate that our atlas is comprehensive (Table S1).

scRNA-seq clusters correspond to morphologically-defined RGC types

To assess the morphology of molecularly-defined RGCs, we applied *in situ* hybridization and IHC to retinas in which RGCs were sparsely labeled (YFP-H line; ~200 RGCs per retina; Samuel et al., 2011). Using genes expressed by one or a few clusters, we validated novel markers for known types and characterized potentially novel types. For example, novel RGC clusters C10 and C24, which specifically expressed *Gpr88* and *Fam19a4*, respectively, possessed dendrites that were bistratified in sublaminae (S)2 and S4 of the inner plexiform layer (IPL), while dendrites of C25, which expressed *Slc17a7* (VGLUT1), stratified exclusively in S5 (Figure 2A). (We divide the IPL into 5 sublaminae, S1–5; Figure 1B). Other examples are shown in Figure S2A–E and results are summarized in Table S2.

Transcriptome-assisted division of RGCs into subclasses

We and others have previously defined several groups of related RGC types, which we call subclasses. They include αRGCs, which express *Spp1* (osteopontin); T- and F-RGCs, defined by expression of the transcription factors *Tbr1* and *Foxp2*, respectively; ooDSGCs, defined by physiological properties and bistratified dendrites; and intrinsically

photosensitive RGCs (ipRGCs), defined by expression of *Opn4* (melanopsin) (Krieger et al., 2017; Liu et al., 2018; Rousso et al., 2016; Schmidt et al., 2011; Vaney et al., 2012) (Table S2). Subclasses exhibit some molecular overlap (for example ON- and OFF-sustained αRGCs express *Opn4* and *Tbr1*, respectively) but are largely distinct.

By double-labeling retinas for a subclass marker and a cluster-specific marker, we validated gene combinations that distinguish RGC types within each of these subclasses. For αRGCs (C41–43,45), the novel marker combinations of the 4 types are more selective than those found previously by a candidate approach (Krieger et al., 2017) (Figures 2B, S2A). Our previous studies identified 4 T-RGC and 4 F-RGC types, but this new approach revealed a fifth type within each subclass (C9 and C32, respectively; Figure 2C,D,S2B). For ipRGCs, we discovered markers for M1 (C33 and 40), M2 (C31) and M4 (C43) types, including some that divide M1-RGCs (identified by high levels of *Opn4* and expression of *Adcyap1*; Hannibal et al., 2002)) into two types (M1a, M1b), as well as an additional cluster (C22) that could correspond to the morphologically and physiologically characterized M3, M5 or M6 types (Figure 2E) (Quattrochi et al., 2019; Schmidt et al., 2011; Stabio et al., 2018; Berg et al., 2019). For ooDSGCs, most of which are *Cartpt+*, we identified the nasal-preferring type (N-ooDSGC) by expression of *Mmp17* but only a single cluster (C16) expressed *Col25a1*, a marker of both D- and V-ooDSGCs (Kay et al., 2011). However, supervised analysis split this cluster with *Calb1* and *Calb2* in largely nonoverlapping cells, bringing the total number of RGC types to 46. Labeling of a line that marks only V-ooDSGCs confirmed that CALB1-positive cells are D-ooDSGCs and CALB2-high cells are V-ooDSGCs (Figure 2F–H).

Another potential subclass is defined by the transgene TYW3, which exhibits insertion site-dependent expression in several types of RGCs that share dendritic lamination in the middle third of the IPL; one is labeled brightly (W3B) and the others dimly (W3D) (Figure S2F) (Kim et al., 2010; Zhang et al., 2012; Krishnaswamy et al., 2015; Laboulaye et al., 2018). We isolated W3-RGCs by FACS and profiled them using Smart-seq2 to obtain deeper coverage (Ding et al., 2019; Picelli et al., 2013). Of 341 RGCs, 97% matched to 1 of 6 types in the atlas: W3B (identified by high expression of Sdk2; Krishnaswamy et al., 2015), F-mini-ON, F-mini-OFF and three others that we call W3D1–3. The remaining 3% corresponded to T-RGC-S2 (Figure S2G,H). Interestingly, all of these types expressed the integral membrane protein *Tusc5/Trarg1* (Figure 2J). Two additional atlas clusters, C1 and C13, were transcriptionally proximate to these types and *Tusc5/Trarg1*-positive; we call them W3-like (W3L) 1 and 2 (Figure 2J). This congruence identifies 9 types as members of a subclass that we provisionally call T5-RGCs. It includes 5 of the 6 most abundant RGC types and accounts for approximately 40% of all RGCs. Collectively, these subclasses account for 26/46 RGC types, with each type occupying no more than two subclasses. Types within a subclass were usually but not always closely related molecularly: 4/5 T-RGCs (*Tbr1+*), 4/5 F-RGCs (*Foxp2+*), 5/9 T5-RGCs (*Tusc5+*), 4/5 ipRGCs (*Opn4+*), and 3/4 αRGCs (*Spp1+*) were close relatives based on a hierarchical clustering analysis (Figure 2J). Our dataset also enabled the identification of a novel subclass based on transcriptional similarity and molecular markers: 8 closely related types co-expressed the transcription factors *Neurod2* and *Satb2* (provisionally N-RGCs; Figure 2J). Types within this group, 7/8 of which are apparently novel, might share cellular characteristics. The remaining 11/45 types were not assigned to a subclass due to the lack of a marker shared with proximal

clusters; but they do exhibit some intriguing transcriptome-wide relationships to other types (Figure 2J). For example, C10 and C24 are transcriptionally proximate to D/V-ooDSGCs (C16) and, like known ooDSGCs, are S2/S4 laminating (Figure 2A); they are candidates for the temporal-preferring (T) ooDSGC type.

RGC types vary dramatically in susceptibility to ONC

Using the adult RGC atlas as a foundation, we assessed the resilience of types to ONC (Figure 3A). To this end, we profiled ~8,500 RGCs 14 days post ONC (dpc), at which point ~80% had died. Extensive injury-related changes in gene expression initially limited our ability to classify surviving RGCs to types using a “one-step” supervised classification framework (Figure 3C). We therefore formulated an alternative approach, leveraging data from RGCs collected at 5 intermediate time points. In this approach, transcriptomic signatures of RGC types were redefined at each time to assign cells at the next time point (Figure 3B). This allowed us to disambiguate gradual injury-related “state” changes from intrinsic type-specific signatures. RGCs were then assigned to types using a hybrid algorithm combining supervised classification (Chen and Guestrin, 2016) and graph-based voting; we call the overall approach iterative-GraphBoost (iGraphBoost; see STAR Methods).

iGraphBoost assigned 89% of total injured RGCs to types, including 77% at 14dpc (Figures 3C). All types maintained expression of *Rbpms* (Figures S3H, I) as well as their specific marker genes through 14dpc (compare Figures 1F and 3D). To visualize the injured RGCs in a 2D representation we combined Liger, which utilizes non-negative matrix factorization (Welch et al., 2019), and t-SNE (Figures S3A). Encouragingly, clusters identified using the Liger representation were associated more strongly with type-specific identities assigned by iGraphBoost, than with other metadata such as time, mouse strain, or collection (Figures S3C). Nonetheless, some surviving RGCs could not be confidently classified. The proportion of “unassigned” cells increased over time, consistent with the idea that injury related transcriptional changes mask type-intrinsic signatures (Figures S3D–F).

We next ranked RGC types by their frequency at 14dpc compared to control (Figure 3E). Survival rates varied continuously from ~1% to ~98%. We refer to the 7 types that showed an increase in relative frequency >2-fold as ‘resilient’ (resRGCs). Because some differences in apparent resilience could result from biases in collection, loss of particularly fragile cells, or misassignment by our computational approach, we also assessed survival for selected types using IHC (Figures S4, S4A–E, Table S3). Histologically and transcriptionally derived frequencies were as highly correlated (Pearson r=.97) at 14dpc (Figure 3H, Table S3), as in controls (Figure 1I). Together, these data provide a comprehensive catalog of type-specific vulnerability of RGCs to injury.

We then asked whether relative resilience of RGC types correlated with overall molecular relationships. In some cases, correspondence was striking. For example, all ipRGC (*Opn4+*) types were resilient, and all N-RGC types were susceptible (Figure 3F). Other transcriptionally defined groupings of RGCs, however, contained types that differed greatly in resilience. For example, among αRGCs, which had previously been characterized as a resilient subclass (Duan et al., 2015), the two sustained types (C42, 43) were highly resilient

but the two transient types (C41, 45) were relatively susceptible, despite transcriptional proximity (Figures 3F, S5A–B). Likewise, both rare and abundant types could be either resilient or vulnerable (Figure 3G). Thus, transcriptional proximity and frequency are imperfect predictors of resilience.

Dynamics of RGC survival after injury define three survival groups

Few RGCs die during the first 3 days after ONC, ~70% die over the next 5 days, and numbers then decline gradually to ~10% survival at 28dpc (Figures 3I, S5F). Based on their kinetics of loss, we partitioned RGC types into three groups: the 7 resilient types (8.1% of control RGCs) declined gradually, reaching ~50% survival at 14dpc; 11 “intermediate” types (27.2% of control RGCs) exhibited a striking decline between 4 and 7dpc; and 27 susceptible types (64.7% of control RGCs) were severely reduced by 4dpc (Figures 3J–M). Thus, survival of the intermediate and susceptible RGCs differed dramatically at 4dpc (susRGCs: 39% ± 21%; intRGCs: 95% ± 25%). Unsurprisingly, these groups correlated well with rankings by survival at 14dpc alone (Figure S3G). As above, we validated scRNAseq-derived survival kinetics of RGC subclasses with distinct survival rates using IHC (Figures S5F–H).

Physiological characteristics of resilient and susceptible RGCs

To determine whether resilient RGCs share functional properties, we monitored physiological characteristics of individual injured RGCs over time, using our recently developed method for *in vivo* recording (Hong et al., 2018). Briefly, a flexible mesh carrying 32 electrodes is injected intravitreally, where it coats the inner retina without disturbing normal eye function; spike sorting protocols identify up to 4 cells per electrode, and provide wave-form signatures that allow longitudinal tracking of the same cell over multiple recording sessions (Figures 4A,B).

We implanted the mesh directly after ONC and recorded RGC activity every 1–2 days for 6–14 days, obtaining data from 142 cells in 4 mice. We used full field illumination and moving gratings to determine whether RGCs exhibited responses that were sustained or transient; orientation-, direction-, or non-selective (OSGCs, DSGCs, and NSGCs, respectively; Figure 4C); and ON, OFF, or ON/OFF (firing in response to luminance increase, decrease or both). At 1dpc, we detected all these functional types, indicating that the method sampled RGC types broadly (Figure 4D).

We then tracked RGCs to identify resilient and susceptible populations. We defined a cell as “dead” if its mean firing rate decreased below 0.5 Hz for at least two consecutive days. ~60% of RGCs died between 3 and 7dpc, with ~74% dead by 14dpc (Figure 4E). In contrast, <10% of cells were lost over two weeks of recordings from uninjured retinas (Hong et al., 2018), indicating that the loss reflects ONC-related death rather than recording instability. Survival dynamics mirror those determined histologically (Figure 3I), suggesting that neurons are not silent for substantial periods prior to their death.

We used this method to ask whether surviving RGCs were enriched for specific response types. RGCs with sustained responses survived ~3-fold better than those with transient responses (Figure 4F), consistent with scRNA-seq results for sustained and transient

αRGCs. Because αRGCs comprise <5% of all RGCs, the physiological result suggests that the relationship between sustained responses and resilience is a general one. OSGCs were more susceptible than DSGCs or NSGCs (Figure 4G). Resilience did not differ between ON or OFF types but ON-OFF types were more vulnerable, independent of feature selectivity (Figure 4H). This vulnerability is consistent with the known susceptibility of ooDGCS, which have transient responses, but did not extend to other DSGCs (Figure 4I). These results reveal a correlation between physiological properties and resilience.

Our longitudinal measurements also enabled the assessment of physiological changes preceding cell death. Overall firing rate of resilient RGCs (those detectable at 14dpc) varied little during the measurement period (Figure 4J). Similarly, for RGCs that died between 3 and 5dpc, the firing rate and orientation- and direction-selectivity indices were largely unchanged between days 1 and 3 (Figures 4K,L). These results suggest that RGCs maintain activity levels and presynaptic inputs, which determine response properties, until shortly before they die.

Morphological changes in resilient and susceptible RGCs

The observation that functional responses of RGCs were retained until at least 48hrs prior to death raised the question as to whether their structural integrity was similarly maintained. We therefore tracked changes in dendritic morphology of 3 resRGC types (ipRGC M2, αRGC OFF-S, and αRGC ON-S/ipRGCC M4) and 3 susRGC types (αRGC OFF-T, and 2 ooDSGC types) after ONC. We used the YFP-H line for sparse labeling in combination with IHC and dendritic lamination to identify types (Figures S5A–C).

Strikingly, resRGCs maintained robust dendritic morphology through 14dpc, with no significant decrease in dendritic area or arbor complexity (Figures 4M,N; S6D,E). Along with functional results, this implies that resRGCs maintain their integrity after ONC. As expected, susRGC types were scarce by 7dpc. Interestingly, however, susRGCs maintained their dendritic area through 4dpc, though their dendrites often appeared thinner and fainter than those in controls and two susRGC types exhibited a significant reduction in dendritic complexity (Figures 4O,P; S6F,G). Together with physiological measurements, this morphological analysis raises the possibility that a substantial window exists during which surviving RGCs could be receptive to regenerative therapies.

Global gene expression changes after ONC

To ask when injury response programs are activated in RGCs, we first characterized the dynamics of globally regulated gene expression after ONC, identifying 771 temporally DE genes that were broadly shared across types (Table S4). Genes were partitioned into 8 modules (Mod1–8) by k-means clustering (Figure 5A), identifying gene sets with distinct temporal dynamics that were enriched for different gene ontology (GO) biological processes (Table S5). For example, module 1 (Mod1), which comprised genes whose expression began to decline by 0.5dpc, was enriched in GO terms associated with functions carried out in healthy neurons such as action potential, synaptic vesicle exo/endocytosis, and retrograde axon transport (Figure 5B). In contrast, Mod5 and Mod6, comprising genes upregulated around 2dpc, were associated with apoptosis and stress pathways (Figure 5C). DE genes

showed few strong type-specific differences, with the notable exception of ipRGC types, which exhibited considerably lower upregulation of Mod5, 6 and 7 genes than other types (Figures 5D–E, S7A–B).

Gene expression correlating with resilience and vulnerability

Next, we next sought type-specific gene expression patterns that correlated with resilience or vulnerability. First, we compared baseline (control) transcriptomic profiles across the three survival groups (Figure 3N). Several genes were expressed in multiple resRGC types but showed little to no expression in susRGC or intRGC types (Figures 5F, S7C). Among them were two IEGs (*Junb* and *Egr1*), enriched in ipRGCs. In light of the upregulation of IEGs by dissociation (Figure S1F), we verified that IEG and other type-specific expression patterns were maintained in RGCs treated with ActD, and are therefore likely to be intrinsic properties (compare Figures 5F and S7D). With the exception of *Igf1*, we found few DE genes that were enriched in all resRGCs but no susRGCs or vice versa, suggesting heterogeneity in factors in mediating resilience or susceptibility across types.

We also asked if resilient and susceptible RGC types up- or down-regulated different sets of genes following injury. As was the case for the analysis at baseline, few genes were up- or down-regulated in all resRGC or susRGC types, but many were upregulated selectively in several resRGC but no susRGC types or vice versa (Figure 5G–J). Thrombospondin 1 was also subtly but specifically upregulated in ipRGCs beginning at 12h post-ONC, consistent with results of Bray et al. (2019). resRGC-enriched genes were generally maintained through 14dpc, suggesting they could play a role in long term survival. In contrast, expression of susRGC-enriched genes generally peaked at 2–4dpc, coincident with the onset of degeneration, suggesting that their expression could be predictive of cell death.

scRNA-seq-derived candidates promote neuroprotection of RGCs

Genes enriched in resRGCs included three previously described mediators of RGC survival and/or axon regeneration: *Igf1* (7/7 resRGCs), *Opn4* (5/7) and *Spp1* (3/7) (Duan et al., 2015; Dupraz et al., 2013; Li et al., 2016; Zhang et al., 2019). To ask whether genes selectively expressed in resilient or susceptible RGC types included additional factors that affected survival, we tested 10 candidates (Table S6). AAV2 vectors were used to overexpress (OE) genes correlating with resilience or to mutate (knock-out, KO) genes correlating with susceptibility. For KO experiments, we infected retinas from *LSL-Cas9* mice crossed to *Vglut2-Cre* mice (to express Cas9 in all RGCs) with vectors encoding a single-guide RNA (sgRNA). We injected AAV intravitreally 14d prior to ONC and quantified RGC survival by IHC at 14dpc (Figure 7A, S8A).

We began with a pair of genes that displayed intriguing expression patterns: urocortin (*Ucn*), which encodes a peptide from the corticotropin-releasing factor family, and corticotropin releasing hormone binding protein (*Crhbp*), a secreted glycoprotein that inhibits UCN-mediated activity (Seasholtz et al., 2002). *Ucn* was upregulated post-ONC in the two sustained αRGC types but not in other RGCs, while *Crhbp* was selectively expressed in multiple susRGC types (Figure 6A,B). The CRH receptor (*Crhr1*), through which UCN signals, was broadly expressed among RGC types (Fig. S8B). We increased *Ucn* levels by

AAV2-based OE or by injection of recombinant protein, and decreased *Crhbp* expression by AAV2-CRISPR-based KO with two different sgRNAs (Figure S8A) All four treatments significantly increased RGC survival (Figure 6C,J, Table S6).

A second pair of related genes was *Timp2*, an inhibitor of matrix metalloproteinases (MMPs) and *Mmp12*, a TIMP2 target (Koppisetti et al., 2014). *Timp2* was selectively enriched in resilient ipRGCs, whereas *Mmp12* was broadly upregulated after ONC but upregulation was particularly modest in ipRGCs (Figure 6D,E). AAV-OE of *Timp2* enhanced survival, as did AAV-KO of *Mmp12* with one of two sgRNAs (Figure 6F, J, Table S6). A small molecule inhibitor selective for MMP12 also improved survival. Because MMPs have overlapping functions, we surveyed the expression of *Mmp*'s in our scRNA-seq data and found that only *Mmp9* was expressed at a detectable level in multiple RGC types (Figure S8C). Targeting *Mmp9* with either of two sgRNAs also improved survival (Figure 6F, J).

Of the other five genes tested, two selectively expressed by resRGCs improved survival: neuron-derived neurotrophic factor, *Ndnf*, which encodes a secretory protein (Kuang et al., 2010), and peripherin, *Prph*, which encodes a neurofilament protein (Thompson and Ziff, 1989) (Figure 6G–J, Table S6). In contrast, KO of three genes enriched in subsets of susRGCs (*Evc2*, *Tac1* and *Hpcal1*) had no significant effect (Figure S8D,E).

Genes would be particularly useful targets if they were able to rescue neurons that do not express them endogenously. We asked whether overexpression of the protective genes *Ucn* and *Timp2* could improve survival of susceptible RGC. To test this idea, we used two markers (CARTPT, NEUROD2) that label susceptible RGC subclasses (Figure 3H), neither of which expresses *Ucn* or *Timp2* at high levels before or after ONC. Both OE-*Ucn* and OE-*Timp2* increased survival of CARTPT+ RGCs but not NEUROD2-RGCs (Figure 6K,L). Thus, these interventions can protect some but not all susceptible RGC types.

Factors correlating with resilience also stimulate axon regeneration

While our screen was focused on neuroprotection, the targets we identified might also promote axon regeneration. To test this possibility, we anterogradely labeled RGC axons by intravitreal injection of fluorescently conjugated cholera toxin B subunit (CTB647) at 12dpc, then counted labeled axons at 14dpc (Figure 7A). OE-*Ucn*, UCN protein, OE-*Timp2*, KO-*Crhbp* and KO-*Mmp9* all promoted significant overall regeneration (Figure 7B,C,E,F, Table S6), with some regenerating axons extending >1500μm. Overexpression of *Ndnf* and *Prph* promoted modest regeneration but only at short distances (Figure 7D,G). These results encourage the hope that our screen will be useful for discovery of targets for axon regeneration as well as neuroprotection.

DISCUSSION

We generated an atlas of adult mouse RGC types, and used it as a foundation to track type-specific responses to injury. We identified a spectrum of resilience among RGC types, and documented transcriptomic, physiological and morphological changes preceding

degeneration. We then manipulated genes selectively expressed in resilient or vulnerable types, finding some that promote RGC survival and axon regeneration following ONC.

An atlas of mouse RGC types

Analysis of 35,699 adult RGC transcriptomes revealed 45 cell clusters. Several lines of evidence indicate that these clusters correspond to cell types: (a) The number of types is similar to those from recent large-scale surveys based on serial section electron microscopy (≥35; Bae et al., 2018), optical imaging of electrical activity (≥32; Baden et al., 2016) and scRNAseq of neonatal retina (40; Rheaume et al., 2018). (b) Several clusters could be assigned to types based on previously known markers. (c) For others, *in situ* hybridization with genes identified from scRNA-seq allowed us to assign clusters to known types or find morphological signatures of previously uncharacterized molecular types. Thus, RGCs join retinal bipolar cells (Shekhar et al., 2016) as a second neuronal class for which transcriptomic criteria tightly correspond to types as defined by classical criteria. This encourages the belief that high-throughput molecular profiling methods, which are currently the most scalable, represent a reliable approach to categorize cell types in the mammalian nervous system.

We cannot, however, be sure that we have captured all RGC types for three reasons. First, our sample size permitted the identification of a type that comprises ~0.15% of all RGCs, but rarer types may have gone undetected. Second, cell dissociation can create biases and fragile types could be missed. Third, V- and D-ooDSGCs formed a single cluster that we split by a semi-supervised analysis, yielding a total of 46 types from 45 clusters. These types are extremely similar; indeed, despite intensive study, no endogenous markers had been found that distinguish them (Kay et al., 2011). They do form separate clusters in early postnatal retina (I.E.W, K.S and J.R.S. in preparation), suggesting that distinguishing genes are downregulated in adulthood. Although supervised analysis of other clusters did not reveal additional subdivisions, we cannot rule out the possibility that other closely related types also co-clustered.

The molecular atlas provided new insights into RGC subclasses. First, for several subclasses previously defined by morphological, physiological or genetic criteria, we identified novel members; e.g., an additional T-RGC and F-RGC. Second, members of a subclass generally showed a global transcriptomic relationship. For example, the T5-RGC types, 6 of which were previously shown to share dendritic lamination, were transcriptomically proximate (5/9 types) and shared expression of *Tusc5*. *Neurod2* and *Satb2* are co-expressed by 8 transcriptomically proximate types, 7 of which are novel. These and other novel types clustering near known types may share cellular features. On the other hand, types that share functional or structural characteristics were not always neighbors on the dendrogram (Figure 2J), particularly when a type was a member of multiple subclasses.

Resilience to injury varies among cell types

To characterize RGC survival after ONC, we applied three independent approaches – scRNA-Seq, IHC, and *in vivo* physiology. We found strong agreement among the criteria in their assessment of type-specific RGC resilience and draw four main conclusions. First,

survival differed dramatically among types, from 1% to 98% over two weeks. Second, types that differed in overall resilience also differed in the time course of death. Third, resilience was not “binary” but rather varied continuously across types. Fourth, in some but not all cases, resilience correlated with molecular or physiological properties of RGC types. For example all 5 ipRGC types were resilient, RGCs with sustained light responses outperformed those with transient responses, and all 8 N-RGC types survived poorly. Nonetheless, we did not find a single characteristic that predicted resilience, suggesting that different resilient neuronal types utilize different survival strategies.

The resilience of sustained RGCs provides an intriguing parallel to patterns of motoneuron survival in Amyotrophic Lateral Sclerosis: the “slow” motoneurons that innervate slow twitch muscle fibers exhibit tonic (~sustained) activity survive better than fast motoneurons, which exhibit phasic (~transient) activity (Pun et al., 2006). This correspondence suggests a general association between firing pattern and resilience, the basis of which remains to be explored.

Cellular changes in neurons with differential resilience

Knowing the kinetics of loss for each RGC type allowed us to characterize molecular, morphological and physiological alterations in the days prior to death. Our main result is that these changes were surprisingly mild up until shortly before somatic loss: dendritic morphology, firing rate and feature selectivity of RGCs remained at close to control levels until at least two days before death. This observation contrasts with models of glaucoma, where dendritic shrinking and functional decline prior to death is striking (Della Santina et al., 2013; Liu et al., 2011). They also seemingly contrast with other studies that observe significant dendritic shrinkage after ONC (e.g., Agostinone et al., 2018); however, those studies focused on broader subclasses of RGCs, so changes in dendritic area could reflect differential survival of RGC types within the subclass being assayed.

Genes that affect resilience and regeneration

As noted above, we found no universal gene expression programs that predicted resilience. We did, however, identify genes expressed selectively by multiple resilient or susceptible types, some of which affect RGC survival and axon regeneration. Among them were two intriguing pairs in which a gene and its antagonist were expressed in opposing populations.

The first pair was *Ucn* and *Crhbp*, expressed by resRGC and susRGCs, respectively. UCN has been shown to promote survival of hippocampal and dopaminergic neurons (Abuirmeileh et al., 2007; Huang et al., 2011; Pedersen et al., 2002). CRHBP binds UCN and prevents it from activating CRHR1 (Seasholtz et al., 2002). The second pair was *Mmp12*, expressed by susRGCs and its endogenous inhibitor, *Timp2* (Dzwonek et al., 2004), expressed by resRGCs. Administration of a soluble inhibitor of MMP12 was recently shown to improve RGC survival after ONC (Vinet et al., 2018), a result we replicated, and *Mmp12* deletion improves recovery from spinal cord injury (Wells et al., 2003) and AAV-mediated gene-transfer of *Timp1* and *Timp2* reduced neuronal damage in transient global ischemia (Magnoni et al., 2007). Overexpression of *Ucn* or *Timp2* improved RGC survival as did KO of *Crhbp* or *Mmp12*.

A guiding hypothesis for this study was that protective genes identified on the basis of their expression by resRGCs would protect other RGC types if expressed broadly. We tested this hypothesis for *Ucn* and *Timp2*, and found that they improved the survival of CARTPT+ RGCs, which are among the most susceptible to ONC. This result supports the idea that targets identified by our methods could be broadly useful. On the other hand, these genes had no effect on survival of another susceptible subclass (NEUROD2+), indicating that neuroprotective strategies may need to be tailored to particular neuronal populations.

Some of the targets identified in our screen for neuroprotection also promoted axon regeneration. These processes are not always linked and can sometimes be antagonistic. For instance, deletion of *Dlk* promotes broad RGC survival but blocks *Pten*-mediated axon regeneration (Watkins et al., 2013), while *Sox11* overexpression promotes long distance axon regeneration in some RGCs but kills others (Norsworthy et al., 2017). Targets that do both are preferable therapeutic candidates in many neurodegenerative contexts.

Distinguishing cell types from cell states

A general question about scRNA-seq- based cell atlases is whether some clusters defined on the basis of transcriptional similarity represent different states of the same cell type rather than different cell types. Because ONC leads to a dramatic but defined change in cell state, our results provided an opportunity to explore this question.

Although injury-related gene expression changes were detectable at 1dpc, cells at this stage could be robustly assigned to type using a “one-step” classifier. At later times, however, classification was increasingly impacted by state-dependent changes. To reliably assign cells to types at late stages, we devised iGraphBoost, which iteratively assigns cells to types using a two-step approach that combines supervised classification and graph-based voting, while updating the model along the time course. We were able to map a high percentage of RGCs accurately even in highly degenerated retina. We expect that this approach will be effective when samples have sufficient temporal resolution to resolve gradual changes in molecular state from intrinsic programs.

In conclusion, mining type-specific molecular correlates of resilience and vulnerability to injury provides a rich source of genes that mediate neuronal survival and axon regeneration. Some of the targets we found are likely to be effective in other contexts, and the general approach is likely to be applicable to other neuronal populations in the CNS.

STAR Methods

LEAD CONTACT AND MATERIALS AVAILABILITY

Further information and requests for resources and reagents should be directed to and will be fulfilled by J.R.S. (sanesj@mcb.harvard.edu). All unique/stable reagents generated in this study are available from the Lead Contact without restriction.

EXPERIMENTAL MODELS AND SUBJECT DETAILS

Mice—All animal experiments were approved by the Institutional Animal Care and Use Committees (IACUC) at Harvard University and Children’s Hospital, Boston. Mice were

maintained in pathogen-free facilities under standard housing conditions with continuous access to food and water. All experiments were carried out in adult mice from 6 to 20 weeks of age and include both males and females. Contribution of gender was not considered in primary analysis, however our meta-analysis of scRNA-Seq variation among samples within a given time point suggest sex-specific differences were a minimal factor (Figure S3C). The following mouse stains were used for both fluorescence activated cell sorting (FACS) and histology: *Vglut2-ires-cre* (*Slc17a6*$^{tm2(cre)Lowl}$*/J*;(Vong et al., 2011)) crossed to the cre-dependent reporter *Thy1-stop-YFP Line#15 (B6.Cg-Tg(Thy1-EYFP)15Jrs/J* (Buffelli et al., 2003), *C57Bl/6J* (JAX # 000664), *TWY3-YFP* (Kim et al., 2010). The following mouse strains were used only for histology: *Kcng4-cre* (Duan et al., 2015) crossed to *Thy1-stop-YFP Line#1* (Buffelli et al., 2003), *Jam-Creer* (Kim et al., 2008) and *Cck-Cre* (Taniguchi et al., 2011) crossed to *Thy1-stop-YFP Line#15, Pv-Cre* (JAX #017320) and *Opn4-Cre* (Ecker et al., 2010) crossed to Rosa-lox-STOP-lox-Tomato (Madisen et al., 2010), *YFP-H* (Feng et al., 2000), *B6.Cg-Tg(Hlxb9-GFP)1Tmj/J (*AKA Hb9-GFP*)* (Kim et al., 2010), *TWY7-YFP* (Kim et al., 2010), and *Penk-cre* (JAX #025112). For Crispr-induced gene knockdown experiments *Vglut2-Cre* crossed to the *Rosa26-LSL-Cas9 knockin* (JAX #024857) was used.

METHOD DETAILS

Unless specified, experiments were not blinded for experimental condition. All experiments were performed on multiple biological replicates to control for natural variation. For scRNA-Seq experiments, appropriate retinal ganglion cell sampling was determined using a 50% down sampling approach, which yielded comparable clustering results. Additional details for cell inclusion for scRNA-Seq experiments are provided in the Computational Methods section below.

Optic Nerve Crush—After anaesthesia with ketamine/xylazine (ketamine 100–120 mg/kg and xylazine 10 mg/kg), we performed optic nerve injury as previously described (Park et al., 2008). Briefly, the optic nerve was exposed intraorbitally and crushed with fine forceps (Dumont #5 FST) for 2s approximately 0.5–1mm behind the optic disc. Eye ointment was applied post-operatively to protect the cornea. All surgeries were performed by an experienced surgeon, who visually confirmed optic nerve crush during the procedure.

Cell preparation and FACS—Retinas were dissected in AMES solution (equilibrated with 95% O2/5% CO2). Upon dissection, eyes and lenses were visually inspected for damage, blood, or inflammation, which were used as criteria for exclusion. Retinas were digested in papain, and dissociated to single cell suspensions using manual trituration in ovomucoid solution. Cells were spun down at 450g for eight minutes, resuspended in AMES +4%BSA to a concentration of 10 million cells per 100µl. 0.5µl of 2µg/µl anti-CD90 (conjugated to various fluorophores) (Thermo Fisher Scientific) per 100µl of cells was incubated for 15 minutes, washed with an excess of media, spun down and resuspended again in AMES+4%BSA at a concentration of ~7 million cells per 1 ml. For Actinomycin-treatment experiments, cell preparation was performed as above and 30µM ActinomycinD (Millipore Sigma) was added to the oxygenated AMES, papain, and ovomucoid solutions. Cells were then resuspended in AMES + 4%BSA + 3µM ActinomycinD. Just prior to FACS the live cell marker calcein blue was added. Cellular debris, doublets, and dead cells

(Calcein Blue negative) were excluded, and RGCs were collected based either on high CD90 expression alone, or on CD90 and GFP co-expression. The former was used when tissue came from C57Bl6/J mice, and the latter when *Vglut2:cre;Stp15* mice were used. Cells were collected into ~100ul of AMES+4%BSA per 25,000 sorted cells. Following collection cells were spun down and resuspended in PBS+0.1% non-acetylated BSA at a concentration range of 500–2000 cells/ul for droplet-based scRNAseq per manufacturer's instructions (10x Chromium). YFP+ RGCs from *TWY3-YFP* were collected in the same way as RGCs from *Vglut2:cre;Stp15* mice, but single cells were sorted into 96 well plates as described below.

RNA-sequencing

3' droplet-based scRNA-seq: Single cell libraries were prepared using the Single-cell gene expression 3' v2 kit on the Chromium platform (10X Genomics, Pleasanton, CA) following the manufacturer's protocol. Briefly, single cells were partitioned into Gel beads in EMulsion (GEMs) in the Chromium instrument followed by cell lysis and barcoded reverse transcription of RNA, amplification, enzymatic fragmentation, 5' adaptor attachment and sample indexing. On average, approximately 8,000–12,000 single cells were loaded on each channel and approximately 3,000–7,000 cells were recovered. Libraries were sequenced on NextSeq 500 or Illumina HiSeq 2500 platforms (Paired end reads: Read 1, 26 bases, Read 2, 98 bases).

W3-YFP Smart-seq2: We profiled 768 single cells from the TYW3 mouse line (Kim et al., 2010), in which a subset of RGCs with S3-laminating dendrites is labeled with YFP. We sorted single YFP+ cells from dissociated retinas into wells of 96-well plates preloaded with 2 µl of lysis buffer containing 0.5% NP-40, 10 mM Tris-HCl, pH 7.6, 0.1 mM EDTA, 2 U/µl RNase Inhibitor (Clontech/TaKaRa). We generated single cell RNA-Seq libraries using a modified Smart-seq2 method (Ding et al., 2019; Picelli et al., 2013) with the following minor change: We added 3 µl instead of 4 µl of master mix containing only 1.7 µl instead of 2.7 µl of 1 M Trehalose (Sigma-Aldrich) directly to the 2 µl cell lysate without a SPRI bead cleanup step. We pooled and sequenced the libraries with paired-end reads (50 bases for read 1 and 25 bases for read 2) on two flowcells with a NextSeq 500 instrument (Illumina).

Histological Methods—Eyes were either collected from animals intracardially perfused with 15–50ml of 4% paraformaldehyde (PFA), and post-fixed for an additional 15 minutes, or dissected from an nonperfused animal and immersion fixed in 4% PFA for 30 minutes. Eyes were transferred to PBS until retinas were dissected, following which retinas were either used for wholemount IHC or sunk in 30% sucrose and embedded in tissue freezing media to cryosection into 20–25µm thick cross-sections. Upon dissection, eyes and lenses were visually inspected for damage, blood, or inflammation, which were used as criteria for exclusion. To immunostain retinal wholemounts, retinas were incubated in protein block (5% normal serum, 0.3% triton-x, 1x PBS) for 3–14 hours, followed by incubation with primary antibodies (in protein block) for 5–7 days in block, and secondary antibodies (in 1x PBS) overnight. All incubations were done at 4°C with gentle rocking. Retinal sections were then used for IHC or fluorescent *in situ* hybridization (FISH). For IHC, slides were incubated for 1 hour in protein block, primary antibody incubation overnight, and secondary antibodies for 2–3 hours. Initial block and secondary antibody incubation were done at room

temperature and primary antibody incubation at 4°C. Probe generation and FISH was performed as described previously with minor modifications (Shekhar et al., 2016), specifically a reduced digestion with Proteinase K (0.5ug/ml for 5 minutes) to preserve the integrity of the GCL. In some cases, FISH was performed using the commercially available RNAscope fluorescent multiplex assay according to manufacturer's instructions, with minor modifications (ACDbio). Specifically, we excluded the step of boiling slides in target retrieval solution, which disrupted IHC staining. Analysis of IHC whole mounts for figures 1, 3, and 4 were single-blinded for sample identity.

Intravitreal injections for manipulation experiments—For AAV-based experiments, mice were anaesthetized with ketamine/xylazine (ketamine 100–120 mg/kg and xylazine 10 mg/kg) and injected intravitreally with ~2μl of volume of AAV2 (in 1x PBS) carrying the gene of interest driven by a CAG promoter, or an sgRNA driven by a U6 promoter, two weeks before crush. Concentration of viruses was adjusted to ~5×10^{12}. Urocortin (rat) protein (Millipore Sigma, ~2μl of 40μM in 1x PBS + 0.1% acetic acid) was injected intravitreally at 2dpc. Mmp12 inhibitor (Mmp408) (Millipore Sigma, ~2μl of 2mM in 1x PBS+1:20 DMSO) was injected intravitreally at 2, 5, 8, 12dpc. For injections, we first removed ~2μl intravitreal fluid from the eye with a sterile micropipette glass. A sterile micropipette glass tip or 33-gauge Hamilton syringe was then inserted through the sclera about 0.5 mm posterior to the limbus and into the vitreal chamber without touching the lens and delivered reagent (~2μl) was injected through the same injection site. After injection, antibiotic ophthalmic ointment was applied and mice stayed warmed on a heating pad until fully awake.

Design of overexpression and knockdown vectors—Boston Children's Hospital Viral Core provided AAV virus. The AAV2-based Crispr/Cas9 approach we employ here has been established as an effective modality for somatic knockdown in adult mouse RGCs (Hung et al., 2016). To account for possible off target effects, we tested two gRNAs per gene, and for added RGC-specificity, we delivered AAV2 single-guide RNA (sgRNA) expression vectors to the eyes of mice that express Cas9 specifically in RGCs (VGlut2-Cre; LSL-Cas9-eGFP), which lead to high infection rates as exemplified here for *Crhbp* sgRNA #2 and OE Ucn (Figure S7A). Vectors and sequences used for manipulation experiments are displayed in Key Resources Table and Table S7.

Anterograde tracing of regenerating axons—To assess axon regeneration, the axons were anterogradely labeled by injecting CTB conjugated with Alexa-647 (Life Technology) via an intravitreal injection 48 hours before sacrifice. After 4% PFA perfusion mice heads were postfixed for 3 hours in 4% PFA. Optic nerves were microdissected and meninges surrounding the nerve were removed. Nerves were then cleared by the protocol provided from Visikol®. In short, the nerves were dehydrated with 100% methanol for 4 minutes and then transferred into Visikol Histo-1 solution for overnight incubation at 4°C. The next day the nerves were inc ubated in Visikol Histo-2 solution for at least 2 hours before mounting them in Visikol Histo-2 solution and imaged with the LSM710 confocal microscope. Optic nerves showing incomplete crushes as evidenced by continuous labeling of axons through

the chiasm and/or a different morphology then regenerating axons (pearls on a string) were excluded from the analysis; they comprised <4% percent of nerves analyzed.

In vivo Electrophysiology

Implantation of mesh electrodes.: Fabrication and non-coaxial implantation of the mesh on the retina surface have been reported by (Hong et al., 2018) except that the mesh electronic probe produced for our experiments carried 32 independently addressable recording electrodes rather than 16 electrodes in the previous report. The mesh was loaded into a sterile borosilicate capillary needle Inner diameter: 200μm, outer diameter: 330μm; Produstrial LLC, Fredon, NJ). Mice were anesthetized by intraperitoneal injection of a mixture of ketamine/xylazine (ketamine 100–120 mg/kg and xylazine 10 mg/kg), the optic nerve of the right eye was crushed as described above and immediately after that a sterile 27-gauge hypodermic needle (BD Technologies, Durham, NC) was used to puncture a hole for sclerotomy below the limbus at the lateral canthus for guiding the insertion of the capillary needle and at the medial canthus for draining the injected liquid to reduce intraocular pressure during injection. Using a stereotactic stage, the capillary needle loaded with the mesh was allowed to advance through the pre-punctured hole at the lateral canthus until its tip reached the nasal part of the retina, taking special caution to avoid damaging the lens. Controlled injection of the mesh electronic neural probe to achieve precise placement was previously reported (Fu et al., 2016; Hong et al., 2018; Hong et al., 2015). After a 2–3mm length of the mesh has been injected and placed on the retina surface, conventional coaxial injection was used while the capillary needle was withdrawn simultaneously, leaving an external portion of the mesh outside the eye. The exit point of the mesh probe in the lateral canthus was secured with a small amount of Kwik-Sil adhesive silicone elastomer (Word Precision Instruments, Sarasota, FL). The medial canthus of the eye was sealed with 3M™Vetbond™Tissue Adhesive (Santa Cruz Biotechnology Inc., Dallas, TX). Antibiotic ointment was applied after eye injection.

The external portion of the mesh has all input/output (I/O) pads, which were unfolded onto a 32-channel flexible flat cable (FFC, #0150200339, Molex, Lisle, IL) for individually addressable I/O connection (Fu et al., 2016; Hong et al., 2018; Hong et al., 2015). After I/O connection, the bonding region of mesh on the FFC was carefully covered with dental cement to the skull with METABOND®. A mouse head-plate, with an opening, for head-fixation during retina recording and visual field stimulation was also cemented to the skull using METABOND®. Additional dental cement was carefully applied to cover the silicone previously applied at the lateral canthus of the injected mouse eye for protection of mesh electronics without touching any part of the mouse eye, eyelids or the mesh, resulting in a monolithic piece of dental cement protecting the mesh electronics and the FFC, and a chronically stable interface for long-term retina electrophysiology.

***In vivo* recording and stimulation protocol.:** We obtained recordings from 4 mice (total of 132 cells) every one or two days, starting from Day 1 following ONC and mesh injection. Mice were placed in a Tailveiner restrainer (Braintree Scientific LLC., Braintree, MA) with the head-plate secured to reduce mechanical noise during recording and fix the visual field of the recorded eye during visual stimulation. The FFC was connected to the signal amplifier

and digitizer (Intan Technologies, Los Angeles, CA) and RGC activities were recorded while visual stimuli were presented to the mouse on a computer screen (20.5″×12.5″), placed a distance of 20cm from both eyes of the mouse, covering an azimuth angle range of ±52°, similar to previously reported protocols (Hong et al., 2018). Recordings were made from the following visual stimuli:

1. F*ull-field ON/OFF stimulation*: A full-field projection of a black screen with 4s duration was followed by a full-field projection of a white screen, with its leading edge entering the screen in eight different directions. The full-field projection of the white screen also lasted 4s, which was followed by another 4s full-field projection of black screen with its leading edge moving in the same direction as the preceding white screen leading edge. Each direction was repeated 10 times.

2. *Moving gratings*: Gratings comprising alternating white and black bars filling the entire computer screen and moving in different directions were programmed in MATLAB. A complete moving grating test comprised 10 repetitive trials, where each trial comprised 8 different directions in a randomized sequence. Baseline was established between repetitions with full-field grey screen, which had the same luminous flux as the alternating white-and-black bars. Gratings moved into each direction for 4 seconds. Data was acquired with a 20-kHz sampling rate and a 60-Hz notch filter.

For recordings during both visual stimulation protocols, data was acquired with a 20-kHz sampling rate and a 60-Hz notch filter.

Computational Methods

Alignment and quantification of gene expression in 3’ droplet-based scRNA-seq data: Demultiplexing and alignment of sequencing reads to the mouse transcriptome (see below) was performed using the Cell Ranger software (version 2.1.0, 10X Genomics). For each sample (i.e. 10X channel/reaction), Cell Ranger generated a matrix of gene counts across cells. We used the option “--forcecells 6000” in “cellranger count” to deliberately extract a larger number of cell barcodes in the data, as we found that the automatic estimate of Cell Ranger was too conservative. Here, 6,000 represented a “loose” upper bound on the number of cells that could be recovered, a value that was calculated from the measured density of the cell suspension loaded onto every channel per the manufacturer’s guidelines.

The 10 samples that were used to assemble the adult RGC atlas (Figure 1) were profiled prior to ONC experiments, and were aligned to the standard mm10 mouse transcriptomic reference that is included in the Cell Ranger suite. For ONC-related scRNA-seq experiments, we aligned the sequence data to an updated transcriptomic reference (see below). The count matrices corresponding to the atlas and the ONC datasets were combined separately to generate consolidated matrices C_{ij} representing the unique molecular identifier (UMI)-based transcript counts for gene i in cell j. For normalization, we first divided each C_{ij} by $\Sigma_i^{\square} C_{ij}$ representing the library size of cell j to obtain a “concentration” matrix $\widetilde{C_{IJ}}$. We then multiplied $\widetilde{C_{IJ}}$ by the median library size M $\left(median_j\left(\Sigma_i^{\square} C_{ij}\right)\right.$ to obtain the

transcripts per median (TPM_{ij} matrix. We defined the normalized expression matrix E_{ij} = (TPM_{ij} + 1).

Updated transcriptome for crush experiments: We obtained high quality total RNA from uninjured control retinas and from a pooled sample of 1, 2, and 14dpc retinas, and processed these separately to generate two (Ctrl and ONC) strand-specific RNA-seq libraries using the TruSeq Total RNA kit (Illumina Inc.). Each library was sequenced on a NextSeq 500 system to obtain 75 million 100bp paired end reads. Next, we used the two datasets to assemble a new mouse retina-specific transcriptomic reference, beginning with the original mm10 mouse reference as a scaffold. We followed a procedure similar to the one we used recently to update a macaque retina transcriptome (Peng et al., 2019). Briefly, following published guidelines (Pertea et al., 2016), we initially mapped the TruSeq reads onto the mm10 transcriptome in a strand-specific manner using the Hisat2 software with command line options "--dta--rna-strandedness RF". Next, we used StringTie v1.3.3 (Pertea et al., 2016) with command line option "--rf" to assemble a new transcriptome based only on the TruSeq reads. After the initial assembly, we reran StringTie with the command line option "--merge" to unify the assembled transcripts with the previous reference to obtain an updated transcriptome annotation. This resulted in modified definitions of transcripts existing in the original reference, as well as novel transcripts supported by the TruSeq reads. While the modified transcripts retained gene names from the original annotation, the novel transcripts were initially named according to Stringtie's naming convention (e.g., MSTRG.7121).

Defining a molecular atlas of mouse RGC types: Our scRNA-seq libraries consisted of three biological replicates (Batch 1–3). In each case, we collected CD90+GFP+ cells from the retinas of Vglut2-cre;Stp15 mice. Cells in Batch 1 were processed in two 10X channels, while cells in Batches 2–3 were processed in four channels each, with an estimated recovery of ~4000–5000 cells per channel. We consolidated the expression matrices, and selected cells where a minimum of 1200 genes were detected. This resulted in a total of 39,750 cells across the three biological replicates (8,091 cells from Batch 1, 17,327 cells from Batch 2 and 14,332 cells from Batch 3).

We identified 1285 highly variable genes $\{g_i\}$ in the data using our previously described Poisson-Gamma model (Pandey et al., 2018) based on the raw count matrix C_{ij}, and used the filtered expression matrix $E_{\{gi\}j}$ for further analysis. We used randomized PCA (Halko et al., 2011) to reduce the dimensionality of the data, and identified 61 statistically significant PCs, identified based on comparison of the empirical eigenspectrum with a "null" spectrum based on the Tracy-Widom distribution, as described earlier (Peng et al., 2019). Next, we built an unweighted k-nearest neighbor (k-NN) graph (k=40) on the cells based on euclidean distance in the 61-dimensional PC space. Each edge connecting a pair of cells i and j was re-weighted using the Jaccard-metric of neighborhood similarity,

$$Edge(i,j) = \frac{\left|Neighborhood_i \cap Neighborhood_j\right|}{\left|Neighborhood_i \cup Neighborhood_j\right|}$$

Where $Neighborhood_i$ denotes the cells that are nearest neighbors of cell i, and |x| denotes the number of elements in the set denoted by x. Using the Infomap algorithm (Rosvall and Bergstrom, 2008), which in our previous experience over-clusters the data (Shekhar et al., 2016), we identified 304 clusters in the data with sizes ranging from 502 cells to 6 cells. We scored each cluster based on cell class-specific signatures for the major retinal neuronal classes - RGCs, Amacrine cells, Photoreceptors, Bipolar cells, Muller glia, horizontal cells, pericytes and microglia (Table S1). Removal of contaminant clusters (Amacrine Cells, Photoreceptors, Immune Cells and Glia) resulted in 251 RGC clusters comprised of 35,699 cells.

While the sensitivity of Infomap was beneficial in identifying, and eliminating contaminants, a large number of the remaining RGC clusters could not be justified based on differential gene expression. In particular, a hierarchical clustering analysis (not shown) revealed a number of instances where multiple clusters were close together in transcriptional space that exhibited minor and graded differences in gene expression, likely representing oversplitting of a single RGC type/state or batch effects. We therefore reclustered the RGCs using the Louvain algorithm (Blondel et al., 2008) applied on a Jaccard-weighted kNN graph (k=30), and applied the iterative approach described earlier (Peng et al., 2019) to identify 45 molecularly distinct clusters (putative RGC types). Through manual inspection of a few Louvain clusters, we confirmed that they were supersets comprised of Infomap clusters that were transcriptionally proximal.

We bootstrapped on the number of genes and number of PCs to ensure that our results were insensitive to variations in these choices (not shown). To further assess the robustness of these clusters, we used the output of two alternatives to PCA to reduce the dimensionality of the data prior to Louvain Clustering - Independent Component Analysis (ICA; (Comon, 1994)) and Liger (Welch et al., 2019), a recently proposed non-negative matrix factorization (NMF; (Lee and Seung, 1999)) based technique based data integration method. Encouragingly, the clusters identified in either space were highly consistent with the results from PCA (Figure S1C,D).

Identifying 2-marker combinations to label RGC types in the atlas: We first identified genes enriched in each RGC type relative to the rest using the MAST framework (Finak et al., 2015). In contrast to our previous study on retinal bipolar cells (Shekhar et al., 2016), we found that most RGC types were not specifically labeled by single genes. We therefore evaluated combinations of two genes on their ability to specifically label cells of a given type.

For each type, we first selected genes that individually showed either a >2-fold enrichment ("+ve markers") or < 2-fold depletion ("-ve markers") compared to the background of other types. Here, fold-enrichment or depletion of gene i was evaluated as the max(r_1, r_2) where,

$$r_1 = \frac{Average\ TPM_{i,\ .}\ across\ cells\ in\ cluster}{Average\ TPM_{i,\ .}\ across\ cells\ in\ background} \text{ and}$$

$$r_2 = \frac{Fraction\ of\ cells\ in\ cluster\ expressing\ gene\ i}{Fraction\ of\ cells\ in\ background\ expressing\ gene\ i}$$

Using these genes, for each RGC type we evaluated (1) all pairwise combinations of +ve markers, and (2) all pairwise combinations consisting of one positive and one negative marker for their ability to specifically label the type based on the area under the precision recall curve (AUCPR). AUCPR is a measure of cluster specificity as described earlier (Pandey et al., 2018). We specifically favored marker combinations that had a higher precision (low proportion of false positives) compared to recall (low proportion of false negatives), as false negatives could arise because of dropouts in scRNA-seq data. The top candidates are displayed in Figure 1F. For few types, we found that it was necessary to screen three marker combinations for achieving higher precision.

Assigning injured RGCs profiled following ONC to types using iGraphBoost: The ONC dataset consisted of cells enriched for RGCs profiled at 6 time points following crush (0.5, 1, 2, 4, 7, and 14dpc), and a separate control dataset (0dpc) independent of the Atlas dataset. We first used an Infomap-based clustering procedure (see above) to remove non-RGCs from the data. he iGraphBoost procedure used to assign injured RGCs to types following ONC was as follows:

Beginning with the RGC atlas as training data, iGraphBoost proceeds by sequentially assigning cells to types at each time point through supervised classification followed by graph-based voting (see below), beginning with 0dpc. Cell type assignments at each timepoint in the ONC dataset are incorporated into a “time point-specific” atlas, which, combined with previous atlases, is used to classify cells at the next time point. This allows us to disambiguate changes in cell state due to injury from the intrinsic molecular distinctions of each RGC type.

Given RGCs atlases at times $t_0, t_1, \ldots, t_i$, we describe here the procedure to assign RGCs at time t_{i+1} to types. Here, t_0 may be regarded as the control RGC atlas and t_1 may be regarded as 0dpc. We train decision-tree based ensemble classifiers Ω_t at each time $t < t_{i+1}$. We tested Random Forests (R package *randomForest*) and Gradient-boosted trees (R package *xgboost*), both yielding consistent results. Results presented were derived from Gradient-boosted trees. Each classifier Ω_t was trained on 70% of cells at time t, and validated on the remaining 30% “held out” cells. The classifier labels were compared to the true labels of the “held out” cells to compute precision and recall values for each of the 45 RGC types. In the assignment of cells at t_{i+1}, a classifier Ω_t’s vote for a class m (when $p^m_{k,t} \geq 0.8$ was only “trusted” if during the validation round both the precision and recall for class m exceeded 0.9.

In **Step 1**, we begin by individually applying the classifiers Ω_t to each cell k at time t_{i+1}. When applied to cell k Ω_t assigns a probability vector $P_{k,t} = (p_{k,t}{}^1, p^2_{k,t}, \ldots, p^{45}_{k,t})$ where $p^m_{k,t}$ is the Ω_t assigned probability that cell k belongs to RGC type m. $p^m_{k,t}$ is the fraction of decision trees in Ω_t that vote for class m. For the classifier Ω_t, we assign cell k to class $m^t = argmax_m p^m_{k,t}$ if and only if $p^{m^t}_{k,t} \geq 0.8$, and Ω_t can be trusted with regards to class m^t (see

above). If $p^{m^t}_{k,t} < 0.8$, we regard cell k as "unassigned" from the point of view of Ω_t. The final assignment of cell k in Step 1 is determined by collectively considering the votes from all the Ω_t such that cell k is assigned to type m if and only if at least one classifier among Ω_t assigns cell k to RGC type m, and the remaining classifiers deem it "unassigned". In cases where two or more classifiers among Ω_t assign cell k to different RGC types, it is deemed "unassigned".

Step 1 resulted in a subset of RGCs at time t_{i+1}being assigned to types with high confidence. In **Step 2**, we use these as "anchors" to propagate labels using the neighborhood relationships. We built a k-nearest neighbor graph on the RGCs with k=15 at t_{i+1} in PCA space, which connects cells based on their transcriptional proximity. We hypothesized that if an unassigned cell's neighbors were predominantly of a single type, this can be used as evidence to assign the transcriptional identity of the unassigned cell. Thus, we iteratively loop through the unassigned cells from Step 1 and assign a cell k to type m, if > 67% of the k=15 nearest neighbors of cell k are of type m. Each iteration decreases the fraction of unassigned cells, and the procedure terminates if the fraction of unassigned cells decreases less than 0.5%. The results were insensitive in variations of the voting threshold between 50% and 80%, although there was a drop in quality outside of these limits. A high voting thresholding (~90%) resulted in a number of unassigned cells, whereas a low voting threshold resulted in a number of spurious assignments, as assessed by post hoc DE analysis. We typically conducted 2–3 "passes" of nearest-neighbor voting, successively propagating labels in the data, stopping when the proportion of newly classified cells was dropped below 1%.

Thus steps 1 and 2 assign type identities RGCs at t_{i+1}. While unassigned cells remained, they were far fewer than the naive "one-step" classification approach, involving a direct assignment of cells based on a classifier Ω_{t0} trained on the atlas (Figure S3).

Finally we summarize features of iGraphBoost that buffer against the forcible assignment of injured RGCs into a preexisting framework. First, in Step 1, iGraphBoost learns type-specific expression patterns from securely classified cells at a previous time point. This should, in principle, incorporate injury related changes that might be type specific to classify cells rather than relying on baseline distinctions. Second, the classification relies on multi-dimensional expression of many markers, making it robust against injury related ectopic changes (loss or gain) in individual markers. Thus, unless RGCs of a given type begin to express a large number of genes characteristic of another type resulting from injury, we do not expect them to be misclassified. Third, the classification process relies on multiple (>1000) decision trees, each trained on a subset of markers. Furthermore, only cells that are assigned to a type by a large majority (>80%) of these decision trees are classified. Fourth, Step 2 of iGraphBoost involves an additional filter in that only cells that have >60% of neighbors of a single type (out of 45) are assigned to that type. Importantly, the classification is not forced upon every cell in that a large number of cells (~25% at 4d,7d and 14d) remain unclassified as their expression signatures. The fidelity of type assignments is demonstrated in Figure 3D, which shows that marker specificity was maintained, though some had lower expression.

Clustering and visualization of atlas and injured RGC transcriptomes: As described previously, we used the PCA coordinates of atlas RGCs to determine clusters using the Louvain-Jaccard algorithm. RGCs were visualized on a 2D map using t-distributed stochastic neighbor embedding (tSNE)(Maaten and Hinton, 2008). We used a recently published scalable implementation of tSNE based on fast interpolation (FI-tSNE) (Linderman et al., 2019).

We initially used a similar procedure to visualize injured RGCs, but found that cells co-clustered by time (Figure S3A), resulting from injury related changes, and to a lesser extent, batch effects (distinct batches from the same time point co-clustered, suggesting that batch-effects were not predominant). We therefore aligned injured RGCs using Liger (Welch et al., 2019), a recently proposed non-negative matrix factorization-based algorithm, to disambiguate shared (RGC type-specific signatures) and dataset-specific (injury related changes) features across the different time points. We used the reduced dimensional coordinates provided by Liger as input for FI-tSNE as well as Louvain-Jaccard clustering (Figure S3A). Compared to tSNE and clusters computed on PC scores, Liger coordinates and clusters were driven far less by time (days post crush or dpc; Figure S3B) compared to iGraphBoost-assigned cell type identity, suggesting that Liger successfully aligns cell types across time. Note that iGraphBoost results did not inform the Liger visualization and clustering).

Comparing relative frequencies of RGC subsets between scRNA-seq and immunohistochemistry: We quantified the frequency of multiple combinatorially labeled subsets of RGCs in retinal whole mounts using immunohistochemistry, and compared them to analogous frequencies quantified using the scRNA-seq data at 0 and 14dpc datasets (Table S3). Frequencies were compared to IHC results, which were quantified as described below.

To compute corresponding frequencies in scRNA-seq, we identified RGC clusters that expressed the genes represented in the IHC combination, and computed their relative frequency in the data at the same time point. For example, to calculate the frequency of *SPP1*$^{+}$*OPN4-cre*$^{-}$ labeled cells in scRNA-seq at 14dpc, we identified all RGC clusters that expressed *Spp1*, but did not express *Opn4* at 14dpc. A cluster was regarded as positively expressing a particular gene if >30% of its cells expressed that gene. For IHC combinations involving a transgene, we used either prior knowledge (e.g. W7) or the analysis reported in this paper (e.g. W3) to identify labeled types in the scRNA-seq. We included the "unassigned" RGCs in the background while computing relative frequencies at any time point. Table S3 describes for each IHC combination, the list of associated types and their corresponding relative frequencies in IHC and scRNA-seq. The procedure to convert estimates of relative frequencies to fractional survival is described below.

Quantifying the survival and kinetics of loss of each type following ONC: Following iGraphBoost, RGCs in the ONC dataset was either assigned to one of 45 types, or were labeled "unassigned". $RF_m(t)$, the relative frequency of RGC type m amongst surviving RGCs at time t was defined as RF_m Here, $N_m(t)$was the number of RGCs assigned to type m at time t, and $U(t)$was the number of unassigned RGCs at time t. $RF_m(t)$ values were used to

calculate the relative frequency ratio for each type m in Figure 3F as $\frac{RF_m(14dpc)}{RF_m(0dpc)}$ To compute the kinetics of loss of each RGC type, we multiplied the relative frequency $RF_m(t)$ of each type with $s(t)$, defined as the *total* fraction of surviving RGCs at each time t, and was estimated independently using IHC (Figure 3I). This enabled us to compute the relative survival ($RS_m(t)$) of each RGC type m,

$$RS_m(t) = \frac{f_m(t)s(t)}{f_m(0)}$$

Individual curves in Figures 3J–L correspond to $FS_m(t)$ for all types. For each type, we obtain a vector $\overrightarrow{RS_m} = \left[RS_m(0dpc), RS_m(0.5dpc), \ldots, RS_m(14dpc)\right]$, where $RS_m(0dpc) = 1$, by construction. We applied k-means clustering to the vectors $\overrightarrow{RS_m}$, and determined 3 clusters by the elbow method. These three clusters corresponded to the survival groups (Figure 3M).

Alignment and quantification of gene expression in full length, plate-based scRNA-seq data: For plate-based libraries, expression levels of gene loci were quantified using RNA-seq by Expectation Maximization (RSEM) (Li and Dewey, 2011). Raw reads were mapped to a mouse transcriptome index (mm10 UCSC build) using Bowtie 2 (Langmead and Salzberg, 2012), as required by RSEM in its default mode. On average, 88% (range 75%-92%) of the reads mapped to the genome in every sample. and 55% (range 20%-66%) of the reads mapped to the transcriptome. RSEM yielded an expression matrix (genes x samples) of inferred gene counts, which was converted to TPM (here, defined as transcripts per million) values and then log-transformed after the addition of 1 to avoid zeros. After filtering cells with low QC metrics (< 400,000 mapped reads, transcriptomic mapping rate < 35% and < 1500 genes detected), we selected 636 cells for further analysis.

Analysis of W3 RGCs: An initial clustering analysis using Louvain-Jaccard clustering on a kNN graph (k=15) in PCA space (17 significant PCs) identified 7 groups of cells comprised of RGCs (n=341), microglia (n=51), bipolar cells (n=9), amacrine (n=67), rods (n=73), doublets involving RGCs and rods (n= 77), and low quality cells (n=18). Next, we separately reclusterd the 341 RGCs using a similar procedure (13 significant PCs), and found 6 clusters. Supervised classification analysis using random forests trained on the atlas data matched 5/6 clusters 1:1 to atlas clusters C2 (W3D1), C4 (F-mini-OFF), C3 (F-mini-ON), C6 (W3B), and C23 (W3D2). The 6 SS2 cluster mapped to C30 (W3D3) and C21 (Tbr1-S2), respectively.

Definition of resRGCs, susRGCs and intRGCs: resRGCs were initially defined as those RGC types m for which $PFR_m > 2$, which included 7 types (C10, C22, C31, C33, C40, C42, C43; see Figure 3E). Independently, as described above, we applied k-means clustering on the vectors $\overrightarrow{FS_m}$, which resulted in the grouping of the 45 RGC types into 3 survival groups. The first cluster comprised the 7 resRGC types. A second cluster comprised 27/45 vulnerable types whose survival rapidly declined by 4dpc, and we called these “susceptible

RGCs" or susRGCs. The other group, consisting of 11/45 types, also exhibited poor survival at 14dpc, but declined more slowly, and were termed "intermediate RGCs" or intRGCs.

Identifying shared differentially expressed genes following ONC, and gene modules: To identify genes that changed significantly across all RGC types, we computed for each gene g its average expression vector $\overrightarrow{E_g} = \left[E_{g,0}, E_{g,0.5}, \ldots, E_{g,14}\right]$, where $E_{g,t}$ represents the average expression strength of gene g across all RGCs at t dpc. We defined $E_{g,t} = P_{g,t}\, avgTPM_{g,t}$, where $P_{g,t}$ represents the fraction of RGCs at time t that express the g, and $avgTPM_{g,t}$ is the average normalized expression of gene g in t dpc RGCs. We excluded genes such that $\min(p_{g,t}) < 0.2$ and $\frac{max_t\left(E_{g,t}\right) - min_t\left(E_{g,t}\right)}{min_t\left(E_{g,t}\right)} < 0.4$, resulting in a total of 3,231 genes.

Next, we randomized the data by shuffling the temporal identities of all RGCs (while maintaining proportions), and computed a randomized average expression vector, $\overrightarrow{E_g^{rand}} = \left[E_{g,0}^{rand}, \ldots, E_{g,14}^{rand}\right]$. We reasoned that genes with significant temporal variation would exhibit larger differences between $\overrightarrow{E_g}$ and $\overrightarrow{E_g^{rand}}$, and therefore computed for each gene g a deviation score between the actual and randomized expression vectors,

$$\Delta_g(\overrightarrow{E_g}, \overrightarrow{E_g^{rand}}) = \frac{\sum_t\left(E_{g,t} - E_{g,t}^{rand}\right)^2}{\sqrt{\frac{\sum_t\left(E_{g,t}+\gamma\right)^2}{T}}\sqrt{\frac{\sum_t\left(E_{g,t}^{rand}+\gamma\right)^2}{T}}}$$

Here, T=7, the total number of time points, and γ represents a pseudocount which we set to 0.2. Here, the denominator acts as a normalizing factor; in its absence we found that genes with higher expression levels were favored. To evaluate the significance of Δ_g values, we used additional randomizations where we computed $\Delta_g^{rand}\left(\overrightarrow{E_g^{rand}_1}, \overrightarrow{E_g^{rand}_2}\right)$ for 10,000 paired randomizations of the data $rand_1$ and $rand_2$, which yielded empirical randomized distributions $P\left(\Delta_g^{rand}\right)$ for each gene g. We found that randomized Δ_g values did not exceed 0.2 for any gene. Based on this, we selected genes g such that $\Delta_g > 0.5$, which yielded 771 genes. We partitioned these genes into 8 modules using k-means clustering on the $\overrightarrow{E_g}$ values (elbow method). To identify biological processes enriched in each module, we applied Gene Ontology (GO) analysis using the R package topGO.

Identifying genes associated with resilient types as targets for manipulation: To identify genes that were selectively enriched in resRGC types at baseline as well as along the time course, we subsampled the data to equalize the representation of each cluster. This was done to reduce the influence of high-frequency types.

We first compared resRGCs vs intRGCs and susRGCs at baseline using the MAST framework (>2-fold, FDR < 0.0001) to identify genes that were selectively enriched in resRGC types at baseline (Figure 5F).

P5 to adult correspondence: To evaluate the molecular correspondence between previously published P5 RGC types (Rheaume et al., 2018) and our adult RGC types, we trained graph-boosted trees on our dataset using a set of common variable genes, and assigned each P5 RGC an adult identity. The P5 cluster labels were not used to train the classifier or inform its assignment. We only considered assignments with voting majoring margin > 50% as valid assignments. The correspondence between P5 cluster labels (as in (Rheaume et al., 2018)) and adult type assignments was high, as evaluated by two measures of cluster similarity, the Adjusted Rand Index and Normalized Mutual Information (Figure S1F).

Data analysis of *in vivo* recordings: The electrophysiological recording data was analyzed offline by two non-blinded researchers using methods described in previous reports (Fu et al., 2016; Hong et al., 2015). In brief, raw recording data was filtered using non-causal Butterworth bandpass filters (‘filtfilt’ function in MATLAB) in the 250–6000 Hz frequency range to extract single-unit spikes of RGCs. Single-unit spike sorting was performed by amplitude thresholding of the filtered traces, where the threshold was automatically determined the threshold based on the median of the background noise according to the improved noise estimation method (Quiroga et al., 2004). Sorted spikes were clustered to determine the number of RGCs and to assign spikes to each RGCbased on principal component analysis (PCA) using the WaveClus software that employs unsupervised superparamagnetic clustering of single-unit spikes.

For each sorted and clustered spike, a firing time was assigned and all spike firing times belonging to the same cluster (i.e., the same RGC) were used to compute the firing rates in response to different visual stimuli. Analysis of single-unit firing events was different for the two different visual stimulation protocols:

1. Full-field ON/OFF stimulation: Firing rate was computed by dividing the number of firing events of the same RGC over time segments for both ON and OFF phases, averaged over 10 trials. Analysis of variance (ANOVA) was performed using the built-in function ‘anova1’ in Matlab to evaluate the statistical significance between firing rates during ON and OFF phases to determine the light response of each recorded RGC.
2. Moving gratings: The number of firing events for a specific moving direction of the grating was averaged over 10 trials, divided by the duration time for each direction to obtain the average firing rate for all eight directions. Angular distribution of firing rates was plotted in the polar plots to reveal direction and orientation preference and selectivity of the recorded RGCs. The direction selectivity index (DSi) is defined as:

$$DSi = \frac{\overline{r_{pref}} - \overline{r_{opp}}}{\overline{r_{pref}} + \overline{r_{opp}}}$$

where $\overline{r_{\text{pref}}}$ and $\overline{r_{\text{opp}}}$ are defined as the average firing rates during moving grating of the preferred direction and that of the opposite direction, respectively. Similarly, the orientation selectivity index (OSi) is defined as:

$$OSi = \frac{\overline{r_{pref}} - \overline{r_{ortho}}}{\overline{r_{pref}} + \overline{r_{ortho}}}$$

where $\overline{r_{\text{pref}}}$ and $\overline{r_{\text{ortho}}}$ are defined as the average firing rates during moving grating of the preferred orientation and that of the orthogonal orientation to the preferred orientation, respectively.

A DSi or OSi of greater than 0.3 is used to assign a specific single unit to DSGC or OSGC, and that of smaller than 0.3 to non-selective ganglion cells (NSGC).

Cross-correlation analysis of spikes trains assigned to neurons belonging to different channels but showing similar direction/orientation selectivity was carried out to identify potential overlap of recording across channels, that is, the same RGC recorded by more than one electrodes, which was removed from the total count of RGCs.

To determine preferential survival of certain functional types through 14dpc in Figure 4F–I, a one-sided Fisher's Exact test was used in R. A p-value smaller than 0.05 were considered statistically significant.

QUANTIFICATION AND STATISTICAL ANALYSIS

Information for statistical analysis for all experiments are provided in figure and table legends. Further details on these statistical approaches are provided below.

Retinal wholemounts—Immunostained retinal whole mounts were imaged using a Zeiss 710 confocal microscope. For RGC subset quantifications a tile scan of the entire ventral quadrant of the retina was taken to control for topological differences in RGC types. The image was processed in ImageJ (Schindelin et al., 2012) by generating a Z-stack maximum projection of the GCL and by applying a local contrast normalization filter (3 stdev). Circular regions-of-interest (ROIs) (8.3μm in diameter) were placed on >500 RGC somas within a longitudinal area spanning the central-peripheral axis. The centroid position and fluorescent intensity of each ROI was measured in ImageJ. Background intensity was determined by selecting a subset of visually confirmed marker negative cells and calculating their linear regression (marker intensity vs. RBPMS intensity). The marker intensity standard deviation was calculated and a linear threshold was set by adding 3x standard deviations to the linear regression y-intercept (Figure S4). Fluorescent intensity for each marker was plotted against RBPMS (total RGCs) in Matlab using customized scripts and thresholded (3x stdev above linear average of negative cells). Thresholded ROIs were then overlaid onto the wholemount images and visually inspected for accuracy and the density for each possible marker combination was measured. To obtain frequency measurements, the density of each marker was divided by the total density (RBPMS). Individual values are shown in Table S3. Established markers and mouse lines that label RGC types or subgroups were selected for quantification before and after ONC. All selected markers/lines label

somas or nuclei of RGC and could be easily distinguished from background signal. Maintenance of expression after ONC was confirmed by IHC and in scRNAseq data. Quantification was performed using a single-blind for sample identity.

For AAV-mediated intervention experiments the maximally infected retinal quadrant was imaged excluding the temporal retina, due to the higher presence of alpha RGCs in this region (Bleckert et al., 2014). Images were processed in ImageJ as previous. Since RGCs at 14dpc are well spaced, it was possible to count them using automated cell segmentation. RGC ROIs were detected using CellProfiler (Carpenter et al., 2006) for the entire retinal quadrant. ROIs were then exported to ImageJ, visually inspected for accuracy, and the intensity and centroid position was measured. To measure marker density, image+ROI overlays were plotted in Matlab and a polygonal boundary region was drawn around the area of the retina that was accurately segmented, taking care to exclude damaged areas, edges where the retina was not viewed en face, and areas with high background staining e.g. blood vessels. Individual values are shown in Table S6. To verify the accuracy of this automated segmentation approach, we re-quantified images previously counted by manual ROI placement and found both approaches gave comparable densities. In assessing survival following interventions, we compared results to four sets of controls. The four were indistinguishable (Figure S8F), so they were averaged for Figure 6J.

Retinal ISH sections—After ISH, sagittal retinal cross sections through or proximal to the optic nerve (maximal width of retina) were imaged using a Zeiss 710 confocal microscope. To quantify markers, a tile scan image spanning the section was generated for ≥4 sections from ≥2 mice. Marker costaining was counted using the ImageJ cell counter plugin. The fraction of each staining combination was recorded and significance determined by two-tailed student's t-test ($p<0.05$).

AAV2 transfection rate—Maximum projections of images acquired also for RGC survival quantifications (see above) from AAV2 OE-Ucn (n=2) and AAV2 Crhbp sgRNA #2 (n=7) were quantified via the ImageJ using the "Analyze particles" function (after applying a threshold for background reduction). After visual inspection to ensure accuracy of cell segmentation, the total number of cells labeled with RBPMS (as panRGC marker) and anti-UCN (IHC staining) or Rbpms and mCherry (AAV2 sgRNA for Crhbp tagged with mCherry to allow direct visualization of virus transfection) was assessed to achieve the percentage of RGCs co-expressing either of them.

Axon regeneration—The cleared, whole nerve was imaged with a 20X air objective. From the center of the nerve, 7 single stacks (2μm stack size) were maximum projected to a total volume of 14μm per nerve. After defining the crush site, lines spaced equidistant from each other at 500-μm intervals from the crush site to where the longest axon could be detected were introduced for bin-by-bin axon quantification. As described previously (Duan et al., 2015; Park et al., 2008), we quantified the total number of regenerating axons, Σad, by using the following formula: $\Sigma ad = \pi r^2 x$ [average axons/mm]/t, where the total number of axons extending distance d in a nerve having a radius of r was estimated by summing over all sections with thickness t (in our case, 14 μm). To assess significance or regeneration, we

used three sets of controls. The three were indistinguishable from each other (Figure S8G), so they were averaged for Figures 7E–G and for statistical analysis.

To assess an effect on regeneration, we first used a definite integral analysis (= area underneath the curve) and then compared each of our interventions to a control injected samples. Significance is determined by two-tailed Student's t-test showing $p < 0.05$ = *. Additionally, bin-by-bin axon quantification was used to assess significant differences between individual distances (500, 1,000, 1,500, 2,000μm), determined by a mixed effects analysis followed by Bonferroni's multiple comparison test with GraphPad Prism, $p < 0.05$ = *. Individual values are shown in Table S6.

Morphometric Analysis—Retinal whole mounts were imaged on an Olympus Fluoview 1000 scanning laser confocal microscope with 20X or 40X oil immersion objectives, optical stacks generated with images taken ever 0.5um. Maximum projections and rotations of images were generated in ImageJ, while brightness and contrast were adjusted in Adobe Photoshop CC. Individual cells were reconstructed and analyzed using the ImageJ plugin Simple Neurite Tracer (SNT, (Longair et al., 2011)). Dendritic size was measured from the area of convex polygons. Dendritic complexity was assessed using total branch points derived from the Stralher analysis in SNT. Significant difference between groups was determined by one-way ANOVA followed by Tukey HSD with SPSS, $p < 0.05$ = *.

DATA AND CODE AVAILABILITY

Submission of all the raw and processed datasets reported in this study has been initiated to the Gene Expression Omnibus (GEO) with accession number GSE137400 (private until publication). The single cell data can be visualized in the Broad Institute's Single Cell Portal at https://singlecell.broadinstitute.org/single_cell/study/SCP509/mouse-retinal-ganglion-cell-adult-atlas-and-optic-nerve-crush-time-series (private until publication), and the code for the ONC analysis is available on https://github.com/klarman-cell-observatory/RetinalGanglionCell-ONC.

Supplementary Material

Refer to Web version on PubMed Central for supplementary material.

ACKNOWLEDGEMENTS

We thank Orenna Brand, Dustin Hermann, Allison Kao, Evan Macosko, Emily Marterskeck, Mu Qiao, Gevin Reynolds, Qingyang Wang and Yaxian Wang for assistance. This work was supported by grants from the NIH (MH105960, EY028625, EY021526, NS029169, NS104248, EY029360, EY028448, EY030204, EY026939, EY028625, P30EY012196 and AG056636), Wings for Life Spinal Cord Research Foundation and sponsored research agreements from Biogen Inc.

REFERENCES

Abuirmeileh A, Lever R, Kingsbury AE, Lees AJ, Locke IC, Knight RA, Chowdrey HS, Biggs CS, and Whitton PS (2007). The corticotrophin-releasing factor-like peptide urocortin reverses key deficits in two rodent models of Parkinson's disease. Eur J Neurosci 26, 417–423. [PubMed: 17650114]

Agostinone J, Alarcon-Martinez L, Gamlin C, Yu WQ, Wong ROL, and Di Polo A (2018). Insulin signalling promotes dendrite and synapse regeneration and restores circuit function after axonal injury. Brain 141, 1963–1980. [PubMed: 29931057]

Aguayo AJ, Rasminsky M, Bray GM, Carbonetto S, McKerracher L, Villegas-Perez MP, Vidal-Sanz M, and Carter DA (1991). Degenerative and regenerative responses of injured neurons in the central nervous system of adult mammals. Philos Trans R Soc Lond B Biol Sci 331, 337–343. [PubMed: 1677478]

Baden T, Berens P, Franke K, Roman Roson M, Bethge M, and Euler T (2016). The functional diversity of retinal ganglion cells in the mouse. Nature 529, 345–350. [PubMed: 26735013]

Bae JA, Mu S, Kim JS, Turner NL, Tartavull I, Kemnitz N, Jordan CS, Norton AD, Silversmith WM, Prentki R, et al. (2018). Digital Museum of Retinal Ganglion Cells with Dense Anatomy and Physiology. Cell 173, 1293–1306 e1219. [PubMed: 29775596]

Belin S, Nawabi H, Wang C, Tang S, Latremoliere A, Warren P, Schorle H, Uncu C, Woolf CJ, He Z, et al. (2015). Injury-induced decline of intrinsic regenerative ability revealed by quantitative proteomics. Neuron 86, 1000–1014. [PubMed: 25937169]

Benowitz LI, He Z, and Goldberg JL (2017). Reaching the brain: Advances in optic nerve regeneration. Exp Neurol 287, 365–373. [PubMed: 26746987]

Berg DJ, Kartheiser K, Leyrer M, Saali A, Berson DM. (2019). Transcriptomic Signatures of Postnatal and Adult Intrinsically Photosensitive Ganglion Cells. eNeuro. 6 pii: ENEURO.0022–19.2019.

Bleckert A, Schwartz GW, Turner MH, Rieke F, and Wong RO (2014). Visual space is represented by nonmatching topographies of distinct mouse retinal ganglion cell types. Curr Biol 24, 310–315. [PubMed: 24440397]

Blondel VD, Guillaume J-L, Lambiotte R, and Lefebvre E (2008). Fast unfolding of communities in large networks. Journal of statistical mechanics: theory and experiment 2008, P10008.

Bray ER, Yungher BJ, Levay K, Ribeiro M, Dvoryanchikov G, Ayupe AC, Thakor K, Marks V, Randolph M, Danzi MC, Schmidt TM, Chaudhari N, Lemmon VP, Hattar S, Park KK (2019) Thrombospondin-1 Mediates Axon Regeneration in Retinal Ganglion Cells. Neuron 103, 642–657. [PubMed: 31255486]

Buffelli M, Burgess RW, Feng G, Lobe CG, Lichtman JW, and Sanes JR (2003). Genetic evidence that relative synaptic efficacy biases the outcome of synaptic competition. Nature 424, 430–434. [PubMed: 12879071]

Carpenter AE, Jones TR, Lamprecht MR, Clarke C, Kang IH, Friman O, Guertin DA, Chang JH, Lindquist RA, Moffat J, et al. (2006). CellProfiler: image analysis software for identifying and quantifying cell phenotypes. Genome Biol 7, R100. [PubMed: 17076895]

Chen T, and Guestrin C (2016). Xgboost: A scalable tree boosting system. Paper presented at: Proceedings of the 22nd acm sigkdd international conference on knowledge discovery and data mining (ACM).

Comon P (1994). Independent component analysis, a new concept? Signal processing 36, 287–314.

Conta Steencken AC, Smirnov I, and Stelzner DJ (2011). Cell survival or cell death: differential vulnerability of long descending and thoracic propriospinal neurons to low thoracic axotomy in the adult rat. Neuroscience 194, 359–371. [PubMed: 21645590]

Della Santina L, Inman DM, Lupien CB, Horner PJ, and Wong RO (2013). Differential progression of structural and functional alterations in distinct retinal ganglion cell types in a mouse model of glaucoma. J Neurosci 33, 17444–17457. [PubMed: 24174678]

Ding J, Adiconis X, Simmons SK, Kowalczyk MS, Hession CC, Marjanovic ND, Hughes TK, Wadsworth MH, Burks T, and Nguyen LT (2019). Systematic comparative analysis of single cell RNA-sequencing methods. BioRxiv, 632216.

Duan X, Qiao M, Bei F, Kim I-J, He Z, and Sanes JR (2015). Subtype-specific regeneration of retinal ganglion cells following axotomy: effects of osteopontin and mTOR signaling. Neuron 85, 1244–1256. [PubMed: 25754821]

Dupraz S, Grassi D, Karnas D, Nieto Guil AF, Hicks D, and Quiroga S (2013). The insulin-like growth factor 1 receptor is essential for axonal regeneration in adult central nervous system neurons. PLoS One 8, e54462. [PubMed: 23349896]

Dzwonek J, Rylski M, and Kaczmarek L (2004). Matrix metalloproteinases and their endogenous inhibitors in neuronal physiology of the adult brain. FEBS Lett 567, 129–135. [PubMed: 15165905]

Ecker JL, Dumitrescu ON, Wong KY, Alam NM, Chen SK, LeGates T, Renna JM, Prusky GT, Berson DM, and Hattar S (2010). Melanopsin-expressing retinal ganglion-cell photoreceptors: cellular diversity and role in pattern vision. Neuron 67, 49–60. [PubMed: 20624591]

Feng G, Mellor RH, Bernstein M, Keller-Peck C, Nguyen QT, Wallace M, Nerbonne JM, Lichtman JW, and Sanes JR (2000). Imaging neuronal subsets in transgenic mice expressing multiple spectral variants of GFP. Neuron 28, 41–51. [PubMed: 11086982]

Finak G, McDavid A, Yajima M, Deng J, Gersuk V, Shalek AK, Slichter CK, Miller HW, McElrath MJ, Prlic M, et al. (2015). MAST: a flexible statistical framework for assessing transcriptional changes and characterizing heterogeneity in single-cell RNA sequencing data. Genome Biol 16, 278. [PubMed: 26653891]

Fu H, Hardy J, and Duff KE (2018). Selective vulnerability in neurodegenerative diseases. Nat Neurosci 21, 1350–1358. [PubMed: 30250262]

Fu TM, Hong G, Zhou T, Schuhmann TG, Viveros RD, and Lieber CM (2016). Stable long-term chronic brain mapping at the single-neuron level. Nat Methods 13, 875–882. [PubMed: 27571550]

Galindo-Romero C, Aviles-Trigueros M, Jimenez-Lopez M, Valiente-Soriano FJ, Salinas-Navarro M, Nadal-Nicolas F, Villegas-Perez MP, Vidal-Sanz M, and Agudo-Barriuso M (2011). Axotomy-induced retinal ganglion cell death in adult mice: quantitative and topographic time course analyses. Exp Eye Res 92, 377–387. [PubMed: 21354138]

Gentleman RC, Carey VJ, Bates DM, Bolstad B, Dettling M, Dudoit S, Ellis B, Gautier L, Ge Y, Gentry J, et al. (2004). Bioconductor: open software development for computational biology and bioinformatics. Genome Biol 5, R80. [PubMed: 15461798]

Halko N, Martinsson P-G, and Tropp JA (2011). Finding structure with randomness: Probabilistic algorithms for constructing approximate matrix decompositions. SIAM review 53, 217–288.

Hannibal J, Hindersson P, Knudsen SM, Georg B, and Fahrenkrug J (2002). The photopigment melanopsin is exclusively present in pituitary adenylate cyclase-activating polypeptide-containing retinal ganglion cells of the retinohypothalamic tract. J Neurosci 22, RC191. [PubMed: 11756521]

Hong G, Fu TM, Qiao M, Viveros RD, Yang X, Zhou T, Lee JM, Park HG, Sanes JR, and Lieber CM (2018). A method for single-neuron chronic recording from the retina in awake mice. Science 360, 1447–1451. [PubMed: 29954976]

Hong G, Fu TM, Zhou T, Schuhmann TG, Huang J, and Lieber CM (2015). Syringe Injectable Electronics: Precise Targeted Delivery with Quantitative Input/Output Connectivity. Nano Lett 15, 6979–6984. [PubMed: 26317328]

Hrvatin S, Hochbaum DR, Nagy MA, Cicconet M, Robertson K, Cheadle L, Zilionis R, Ratner A, Borges-Monroy R, Klein AM, et al. (2018). Single-cell analysis of experience-dependent transcriptomic states in the mouse visual cortex. Nat Neurosci 21, 120–129. [PubMed: 29230054]

Huang HY, Lin SZ, Chen WF, Li KW, Kuo JS, and Wang MJ (2011). Urocortin modulates dopaminergic neuronal survival via inhibition of glycogen synthase kinase-3beta and histone deacetylase. Neurobiol Aging 32, 1662–1677. [PubMed: 19875195]

Huebner EA, and Strittmatter SM (2009). Axon regeneration in the peripheral and central nervous systems. Results Probl Cell Differ 48, 339–351. [PubMed: 19582408]

Hung SS, Chrysostomou V, Li F, Lim JK, Wang JH, Powell JE, Tu L, Daniszewski M, Lo C, Wong RC, et al. (2016). AAV-Mediated CRISPR/Cas Gene Editing of Retinal Cells In Vivo. Invest Ophthalmol Vis Sci 57, 3470–3476. [PubMed: 27367513]

Kaplan A, Spiller KJ, Towne C, Kanning KC, Choe GT, Geber A, Akay T, Aebischer P, and Henderson CE (2014). Neuronal matrix metalloproteinase-9 is a determinant of selective neurodegeneration. Neuron 81, 333–348. [PubMed: 24462097]

Kay JN, De la Huerta I, Kim IJ, Zhang Y, Yamagata M, Chu MW, Meister M, and Sanes JR (2011). Retinal ganglion cells with distinct directional preferences differ in molecular identity, structure, and central projections. J Neurosci 31, 7753–7762. [PubMed: 21613488]

Kim IJ, Zhang Y, Meister M, and Sanes JR (2010). Laminar restriction of retinal ganglion cell dendrites and axons: subtype-specific developmental patterns revealed with transgenic markers. J Neurosci 30, 1452–1462. [PubMed: 20107072]

Kim IJ, Zhang Y, Yamagata M, Meister M, and Sanes JR (2008). Molecular identification of a retinal cell type that responds to upward motion. Nature 452, 478–482. [PubMed: 18368118]

Kim D, Paggi JM, Park C, Bennett C, Salzberg SL (2019). Graph-based genome alignment and genotyping with HISAT2 and HISAT-genotype. Nat Biotechn 37, 907–915.

Kizil C, Kaslin J, Kroehne V, and Brand M (2012). Adult neurogenesis and brain regeneration in zebrafish. Dev Neurobiol 72, 429–461. [PubMed: 21595047]

Koppisetti RK, Fulcher YG, Jurkevich A, Prior SH, Xu J, Lenoir M, Overduin M, and Van Doren SR (2014). Ambidextrous binding of cell and membrane bilayers by soluble matrix metalloproteinase-12. Nat Commun 5, 5552. [PubMed: 25412686]

Krieger B, Qiao M, Rousso DL, Sanes JR, and Meister M (2017). Four alpha ganglion cell types in mouse retina: Function, structure, and molecular signatures. PLoS One 12, e0180091. [PubMed: 28753612]

Krishnaswamy A, Yamagata M, Duan X, Hong YK, and Sanes JR (2015). Sidekick 2 directs formation of a retinal circuit that detects differential motion. Nature 524, 466–470. [PubMed: 26287463]

Kuang XL, Zhao XM, Xu HF, Shi YY, Deng JB, and Sun GT (2010). Spatio-temporal expression of a novel neuron-derived neurotrophic factor (NDNF) in mouse brains during development. BMC Neurosci 11, 137. [PubMed: 20969804]

Laboulaye MA, Duan X, Qiao M, Whitney IE, and Sanes JR (2018). Mapping Transgene Insertion Sites Reveals Complex Interactions Between Mouse Transgenes and Neighboring Endogenous Genes. Front Mol Neurosci 11, 385. [PubMed: 30405348]

Langmead B, and Salzberg SL (2012). Fast gapped-read alignment with Bowtie 2. Nat Methods 9, 357–359. [PubMed: 22388286]

Lee DD, and Seung HS (1999). Learning the parts of objects by non-negative matrix factorization. Nature 401, 788–791. [PubMed: 10548103]

Li B, and Dewey CN (2011). RSEM: accurate transcript quantification from RNA-Seq data with or without a reference genome. BMC bioinformatics 12, 323. [PubMed: 21816040]

Li S, Yang C, Zhang L, Gao X, Wang X, Liu W, Wang Y, Jiang S, Wong YH, Zhang Y, et al. (2016). Promoting axon regeneration in the adult CNS by modulation of the melanopsin/GPCR signaling. Proc Natl Acad Sci U S A 113, 1937–1942. [PubMed: 26831088]

Linderman GC, Rachh M, Hoskins JG, Steinerberger S, and Kluger Y (2019). Fast interpolation-based t-SNE for improved visualization of single-cell RNA-seq data. Nat Methods 16, 243–245. [PubMed: 30742040]

Liu J, Reggiani JDS, Laboulaye MA, Pandey S, Chen B, Rubenstein JLR, Krishnaswamy A, and Sanes JR (2018). Tbr1 instructs laminar patterning of retinal ganglion cell dendrites. Nat Neurosci 21, 659–670. [PubMed: 29632360]

Liu M, Duggan J, Salt TE, and Cordeiro MF (2011). Dendritic changes in visual pathways in glaucoma and other neurodegenerative conditions. Exp Eye Res 92, 244–250. [PubMed: 21310146]

Longair MH, Baker DA, and Armstrong JD (2011). Simple Neurite Tracer: open source software for reconstruction, visualization and analysis of neuronal processes. Bioinformatics 27, 2453–2454. [PubMed: 21727141]

Maaten L.v.d., and Hinton G (2008). Visualizing data using t-SNE. Journal of machine learning research 9, 2579–2605.

Maclaren RE, and Taylor JS (1997). Regeneration in the developing optic nerve: correlating observations in the opossum to other mammalian systems. Prog Neurobiol 53, 381–398. [PubMed: 9364617]

Macosko EZ, Basu A, Satija R, Nemesh J, Shekhar K, Goldman M, Tirosh I, Bialas AR, Kamitaki N, and Martersteck EM (2015). Highly parallel genome-wide expression profiling of individual cells using nanoliter droplets. Cell 161, 1202–1214. [PubMed: 26000488]

Madisen L, Zwingman TA, Sunkin SM, Oh SW, Zariwala HA, Gu H, Ng LL, Palmiter RD, Hawrylycz MJ, Jones AR, et al. (2010). A robust and high-throughput Cre reporting and characterization system for the whole mouse brain. Nat Neurosci 13, 133–140. [PubMed: 20023653]

Magnoni S, Baker A, Thomson S, Jordan G, George SJ, McColl BW, McCulloch J, and Horsburgh K (2007). Neuroprotective effect of adenoviral-mediated gene transfer of TIMP-1 and -2 in ischemic brain injury. Gene Ther 14, 621–625. [PubMed: 17235293]

McLean JR, Smith GA, Rocha EM, Osborn TM, Dib S, Hayes MA, Beagan JA, Brown TB, Lawson TF, Hallett PJ, et al. (2014). ALS-associated peripherin spliced transcripts form distinct protein inclusions that are neuroprotective against oxidative stress. Exp Neurol 261, 217–229. [PubMed: 24907400]

Norsworthy MW, Bei F, Kawaguchi R, Wang Q, Tran NM, Li Y, Brommer B, Zhang Y, Wang C, Sanes JR, et al. (2017). Sox11 Expression Promotes Regeneration of Some Retinal Ganglion Cell Types but Kills Others. Neuron 94, 1112–1120 e1114. [PubMed: 28641110]

Pandey S, Shekhar K, Regev A, and Schier AF (2018). Comprehensive Identification and Spatial Mapping of Habenular Neuronal Types Using Single-Cell RNA-Seq. Curr Biol 28, 1052–1065 e1057. [PubMed: 29576475]

Park KK, Liu K, Hu Y, Smith PD, Wang C, Cai B, Xu B, Connolly L, Kramvis I, Sahin M, et al. (2008). Promoting axon regeneration in the adult CNS by modulation of the PTEN/mTOR pathway. Science 322, 963–966. [PubMed: 18988856]

Pedersen WA, Wan R, Zhang P, and Mattson MP (2002). Urocortin, but not urocortin II, protects cultured hippocampal neurons from oxidative and excitotoxic cell death via corticotropin-releasing hormone receptor type I. J Neurosci 22, 404–412. [PubMed: 11784785]

Peng YR, Shekhar K, Yan W, Herrmann D, Sappington A, Bryman GS, van Zyl T, Do MTH, Regev A, and Sanes JR (2019). Molecular Classification and Comparative Taxonomics of Foveal and Peripheral Cells in Primate Retina. Cell 176, 1222–1237 e1222. [PubMed: 30712875]

Perez de Sevilla Muller L, Sargoy A, Rodriguez AR, and Brecha NC (2014). Melanopsin ganglion cells are the most resistant retinal ganglion cell type to axonal injury in the rat retina. PLoS One 9, e93274. [PubMed: 24671191]

Pertea M, Kim D, Pertea GM, Leek JT, and Salzberg SL (2016). Transcript-level expression analysis of RNA-seq experiments with HISAT, StringTie and Ballgown. Nature protocols 11, 1650. [PubMed: 27560171]

Picelli S, Björklund ÅK, Faridani OR, Sagasser S, Winberg G, and Sandberg R (2013). Smart-seq2 for sensitive full-length transcriptome profiling in single cells. Nature methods 10, 1096. [PubMed: 24056875]

Pun S, Santos AF, Saxena S, Xu L, and Caroni P (2006). Selective vulnerability and pruning of phasic motoneuron axons in motoneuron disease alleviated by CNTF. Nat Neurosci 9, 408–419. [PubMed: 16474388]

Quattrochi LE, Stabio ME, Kim I, Ilardi MC, Michelle Fogerson P, Leyrer ML, and Berson DM (2019). The M6 cell: A small-field bistratified photosensitive retinal ganglion cell. J Comp Neurol 527, 297–311. [PubMed: 30311650]

Quiroga RQ, Nadasdy Z, and Ben-Shaul Y (2004). Unsupervised spike detection and sorting with wavelets and superparamagnetic clustering. Neural Comput 16, 1661–1687. [PubMed: 15228749]

Rheaume BA, Jereen A, Bolisetty M, Sajid MS, Yang Y, Renna K, Sun L, Robson P, and Trakhtenberg EF (2018). Single cell transcriptome profiling of retinal ganglion cells identifies cellular subtypes. Nat Commun 9, 2759. [PubMed: 30018341]

Ross SE, McCord AE, Jung C, Atan D, Mok SI, Hemberg M, Kim TK, Salogiannis J, Hu L, Cohen S, et al. (2012). Bhlhb5 and Prdm8 form a repressor complex involved in neuronal circuit assembly. Neuron 73, 292–303. [PubMed: 22284184]

Rosvall M, and Bergstrom CT (2008). Maps of random walks on complex networks reveal community structure. Proc Natl Acad Sci U S A 105, 1118–1123. [PubMed: 18216267]

Rousso DL, Qiao M, Kagan RD, Yamagata M, Palmiter RD, and Sanes JR (2016). Two Pairs of ON and OFF Retinal Ganglion Cells Are Defined by Intersectional Patterns of Transcription Factor Expression. Cell Rep 15, 1930–1944. [PubMed: 27210758]

Samuel MA, Zhang Y, Meister M, and Sanes JR (2011). Age-related alterations in neurons of the mouse retina. J Neurosci 31, 16033–16044. [PubMed: 22049445]

Sanes JR, and Masland RH (2015). The types of retinal ganglion cells: current status and implications for neuronal classification. Annu Rev Neurosci 38, 221–246. [PubMed: 25897874]

Saxena S, and Caroni P (2011). Selective neuronal vulnerability in neurodegenerative diseases: from stressor thresholds to degeneration. Neuron 71, 35–48. [PubMed: 21745636]

Schindelin J, Arganda-Carreras I, Frise E, Kaynig V, Longair M, Pietzsch T, Preibisch S, Rueden C, Saalfeld S, Schmid B, et al. (2012). Fiji: an open-source platform for biological-image analysis. Nat Methods 9, 676–682. [PubMed: 22743772]

Schmidt TM, Do MT, Dacey D, Lucas R, Hattar S, and Matynia A (2011). Melanopsin-positive intrinsically photosensitive retinal ganglion cells: from form to function. J Neurosci 31, 16094–16101. [PubMed: 22072661]

Seasholtz AF, Valverde RA, and Denver RJ (2002). Corticotropin-releasing hormone-binding protein: biochemistry and function from fishes to mammals. J Endocrinol 175, 89–97. [PubMed: 12379493]

Shekhar K, Lapan SW, Whitney IE, Tran NM, Macosko EZ, Kowalczyk M, Adiconis X, Levin JZ, Nemesh J, and Goldman M (2016). Comprehensive classification of retinal bipolar neurons by single-cell transcriptomics. Cell 166, 1308–1323. e1330. [PubMed: 27565351]

Stabio ME, Sabbah S, Quattrochi LE, Ilardi MC, Fogerson PM, Leyrer ML, Kim MT, Kim I, Schiel M, Renna JM, Briggman KL, Berson DM. (2018). The M5 Cell: A Color-Opponent Intrinsically Photosensitive Retinal Ganglion Cell. Neuron. 97:150–163. [PubMed: 29249284]

Taniguchi H, He M, Wu P, Kim S, Paik R, Sugino K, Kvitsiani D, Fu Y, Lu J, Lin Y, et al. (2011). A resource of Cre driver lines for genetic targeting of GABAergic neurons in cerebral cortex. Neuron 71, 995–1013. [PubMed: 21943598]

Thompson MA, and Ziff EB (1989). Structure of the gene encoding peripherin, an NGF-regulated neuronal-specific type III intermediate filament protein. Neuron 2, 1043–1053. [PubMed: 2624740]

Vaney DI, Sivyer B, and Taylor WR (2012). Direction selectivity in the retina: symmetry and asymmetry in structure and function. Nat Rev Neurosci 13, 194–208. [PubMed: 22314444]

Vinet J, Costa AM, Salinas-Navarro M, Leo G, Moons L, Arckens L, and Biagini G (2018). A Hydroxypyrone-Based Inhibitor of Metalloproteinase-12 Displays Neuroprotective Properties in Both Status Epilepticus and Optic Nerve Crush Animal Models. Int J Mol Sci 19.

Vong L, Ye C, Yang Z, Choi B, Chua S Jr., and Lowell BB (2011). Leptin action on GABAergic neurons prevents obesity and reduces inhibitory tone to POMC neurons. Neuron 71, 142–154. [PubMed: 21745644]

Watkins TA, Wang B, Huntwork-Rodriguez S, Yang J, Jiang Z, Eastham-Anderson J, Modrusan Z, Kaminker JS, Tessier-Lavigne M, and Lewcock JW (2013). DLK initiates a transcriptional program that couples apoptotic and regenerative responses to axonal injury. Proc Natl Acad Sci U S A 110, 4039–4044. [PubMed: 23431164]

Welch JD, Kozareva V, Ferreira A, Vanderburg C, Martin C, and Macosko EZ (2019). Single-Cell Multi-omic Integration Compares and Contrasts Features of Brain Cell Identity. Cell 177, 1873–1887 e1817. [PubMed: 31178122]

Welin D, Novikova LN, Wiberg M, Kellerth JO, and Novikov LN (2008). Survival and regeneration of cutaneous and muscular afferent neurons after peripheral nerve injury in adult rats. Exp Brain Res 186, 315–323. [PubMed: 18057922]

Wells JE, Rice TK, Nuttall RK, Edwards DR, Zekki H, Rivest S, and Yong VW (2003). An adverse role for matrix metalloproteinase 12 after spinal cord injury in mice. J Neurosci 23, 10107–10115. [PubMed: 14602826]

Wu YE, Pan L, Zuo Y, Li X, and Hong W (2017). Detecting Activated Cell Populations Using Single-Cell RNA-Seq. Neuron 96, 313–329 e316. [PubMed: 29024657]

Zhang Y, Kim IJ, Sanes JR, and Meister M (2012). The most numerous ganglion cell type of the mouse retina is a selective feature detector. Proc Natl Acad Sci U S A 109, E2391–2398. [PubMed: 22891316]

Zhang Y, Williams PR, Jacobi A, Wang C, Goel A, Hirano AA, Brecha NC, Kerschensteiner D, and He Z (2019). Elevating Growth Factor Responsiveness and Axon Regeneration by Modulating Presynaptic Inputs. Neuron (in press).

Highlights

- 46 transcriptionally distinct type of retinal ganglion cells (RGCs) in mice
- RGC types differ dramatically in survival following axonal transection
- Different genes expressed by resilient and vulnerable RGC types
- Manipulation of differentially expressed genes promotes RGC survival and regeneration

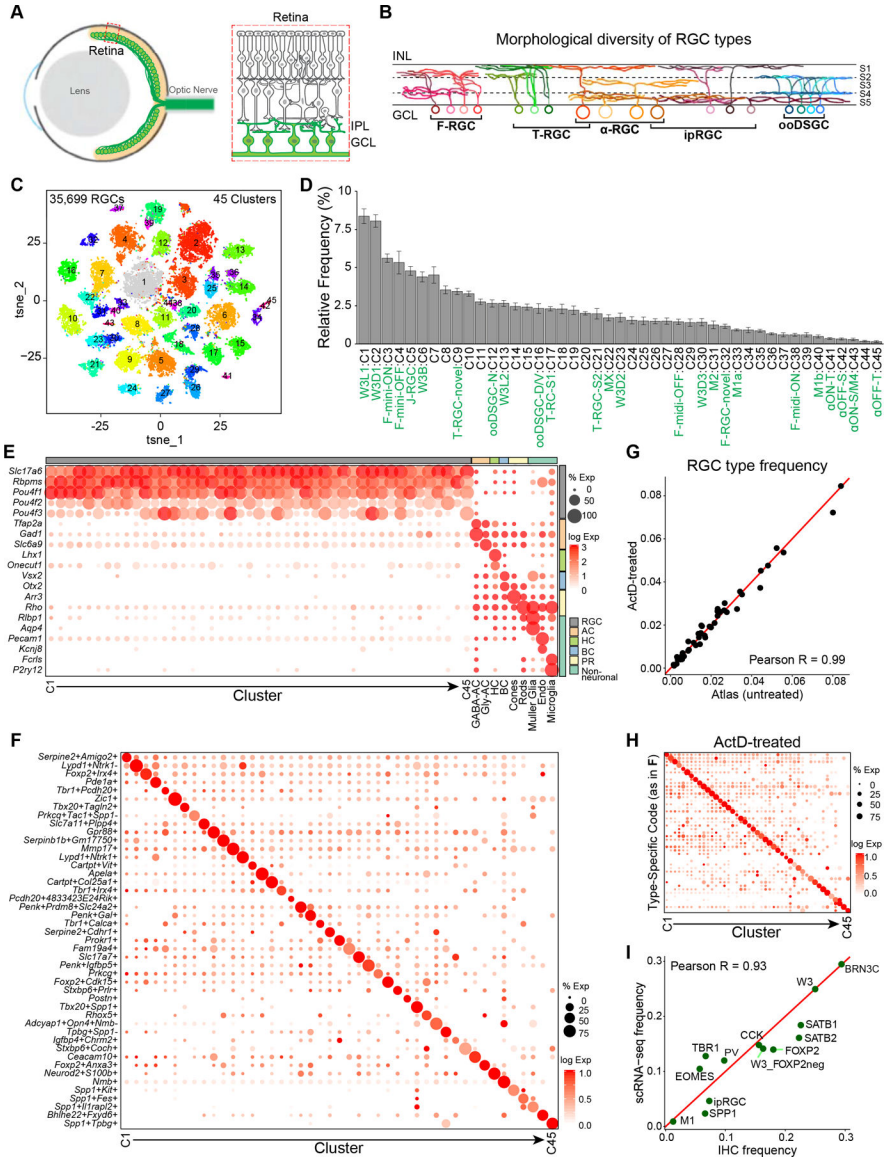

Figure 1. scRNA-seq reveals 45 molecularly distinct RGC types in adult mice

A. RGCs (green) reside within the innermost layer of the retina, the ganglion cell layer (GCL). Their axons bundle together to form the optic nerve. IPL, inner plexiform layer, GCL, ganglion cell layer.

B. Dendrites of different RGC types have distinct lamination patterns within sublaminae (S)1–5 of the IPL, which determines their choice of presynaptic partners. Stereotyped morphologies are illustrated here for several RGC subclasses and types. INL, inner nuclear layer.

C. t-distributed stochastic neighbor embedding (t-SNE) visualization of the transcriptional heterogeneity of 35,699 adult mouse RGCs. Cells are colored by cluster assignments, determined using graph clustering. Clusters are numbered in order of decreasing frequency.

D. Relative frequencies of RGC clusters C1–45 (mean ±SD, n=10 replicates). Clusters that matched to known types or subclasses are labeled.

E. Dotplot showing the expression patterns of marker genes (rows) specific to different retinal classes across RGC and non-RGC clusters in the data (columns; see color bars, top and right). The size of each circle is proportional to the percentage of cells expressing the gene, and the color depicts the average normalized transcript count in expressing cells. GABA-AC and Gly-AC, GABAergic and glycinergic amacrine cells; HC, horizontal cells; BC, bipolar cells; PR, photoreceptors; Endo, endothelial cells.

F. Dotplot showing gene combinations (rows) that uniquely mark RGC clusters (columns). Representation as in panel E for single genes, here normalized to 1. 2- or 3- marker codes, always involve the presence of a marker *A*, and the presence (e.g. *A*+*B*+ or *A*+*B*+*C*+) or absence (e.g. *A*+*B*-, or *A*+*B*-*C*+) of markers *B* and *C*. In such cases, the size of the circle indicates the percentage of cells satisfying the expression pattern, and the color depicts the average transcript count of positive markers in the cells, normalized to 1 for each combination.

G. RGC type frequencies are highly similar between ActinomycinD (ActD)-treated (y-axis) and atlas (x-axis) retinas.

H. Dotplot showing gene combinations that uniquely define each RGC type in nominal controls (as in **F**), are preserved in ActD-treated retinas. Row and column order as in **F**.

I. Scatter plot showing tight correspondence ($R_{Pearson}$ = 0.93) between relative frequencies of RGC groups found by scRNA-seq (y-axis) versus IHC (x-axis).

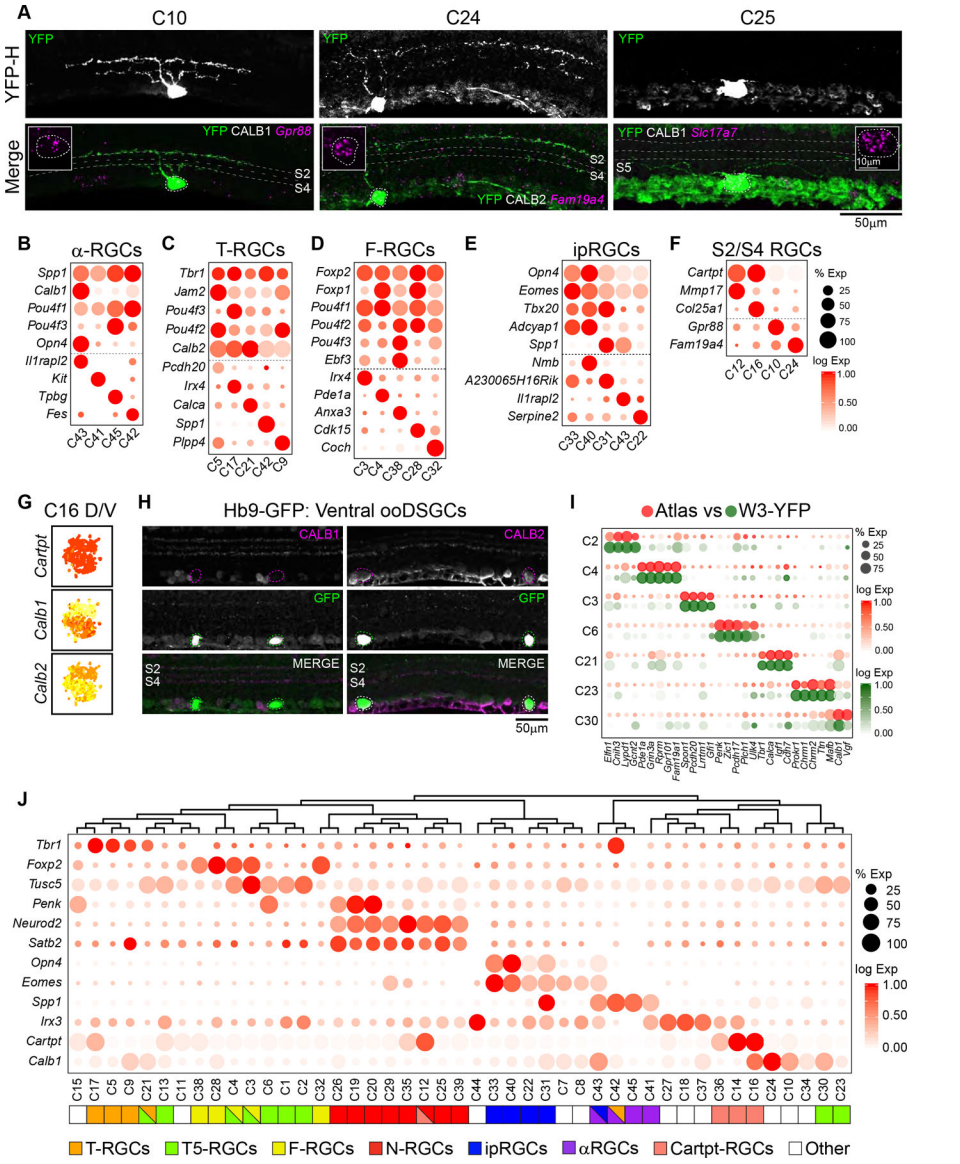

Figure 2. Correspondence of scRNA-seq clusters to RGC types

A. Characterization of novel RGC types by combining FISH (magenta) and IHC on sparsely labeled RGCs in the YFP-H line (green). Examples of S2/S4 laminating C10 and C24 RGCs expressing *Gpr88* (left) and *Fam19a4* (middle), respectively, and an S5 laminating C25 RGC expressing *Slc17a7* (right). IPL sublaminae are drawn based on CALB1 or CALB2 staining (white dashed lines). YFP-H line. Examples of S2/S4 laminating C10 and C24 RGCs expressing Gpr88 (left) and Fam19a4 (middle), respectively, and an S5 laminating C25 RGC expressing Slc17a7 (right). IPL sublaminae are drawn based on CALB1 or CALB2 staining (white dashed lines). Merge in “C25” panel shows labeled cell at higher gain to reveal dendritic morphology.

B-F Dotplots highlighting transcriptional distinctions among RGC types within subclasses. Dotted lines separate previously described markers (above) from novel markers identified in

this study (below). B: αRGC types. C: T-RGC types. D: F-RGC types. E: ipRGC types. F: S2/S4 laminating RGC types.

G. C16 comprising D/V-ooDSGCs can be partitioned into *Calb1*+ (putative D-ooDSGCs) and *Calb1*- (putative V-ooDSGCs) cells.

H. Consistent with the interpretation in panel G, GFP+ cells in the *Hb9* mouse line, which labels V-ooDSGCs, are CALB1- and CALB2+ (magenta).

I. Dotplot showing consistent patterns of DE gene expression between W3 types (rows) detected in the droplet-based scRNA-seq atlas (red) and plate-based data from FACS-sorted W3 RGCs (green). Labeled by atlas cluster id.

J. Transcriptional relatedness of RGC clusters visualized as a dendrogram reveals subclasses of RGC types (annotation bar, bottom). Dotplot shows expression of key subclass-enriched or -defining genes (rows) in clusters (columns).

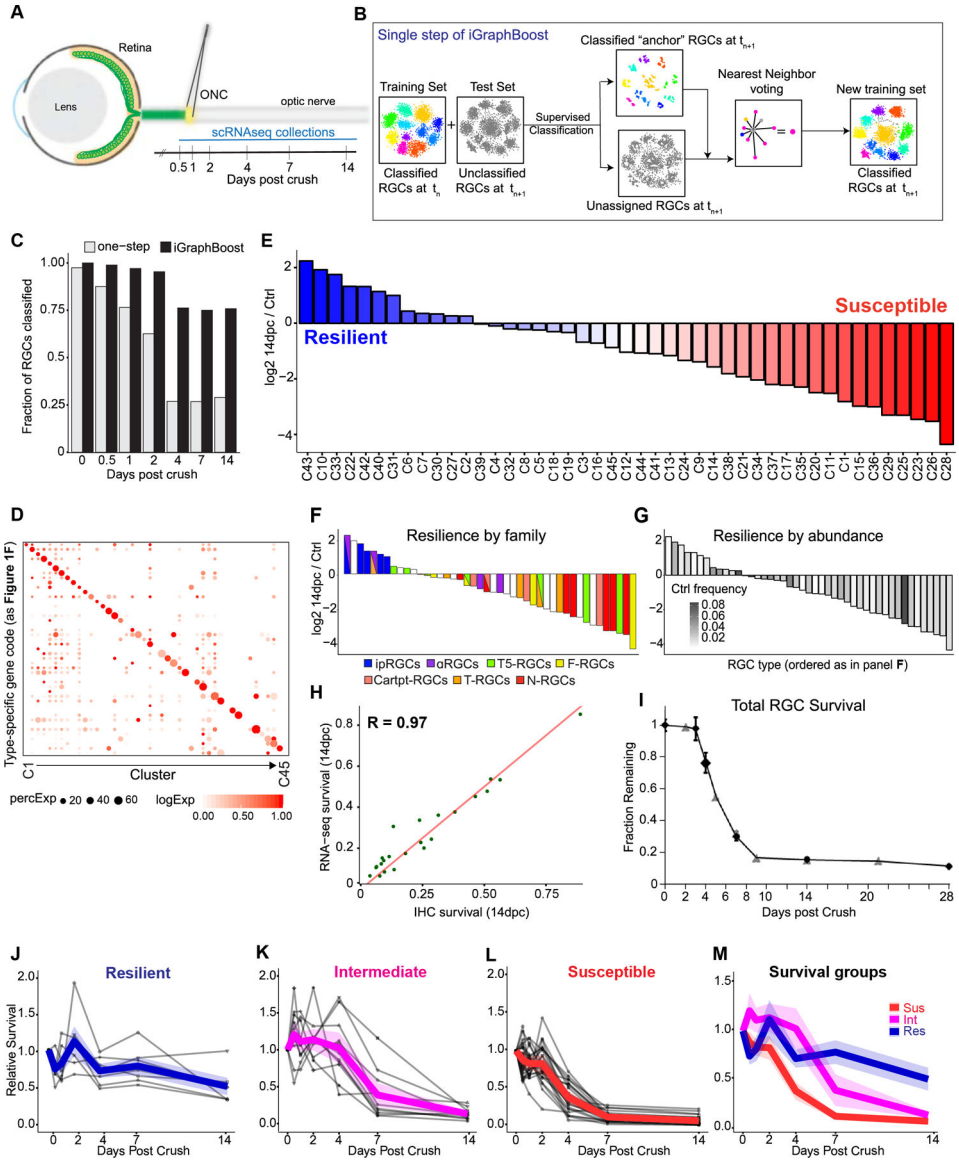

Figure 3. scRNA-seq profiling of RGCs following ONC

A. scRNA-seq was performed on RGCs collected before and at six times following ONC. 8,456–13,619 RGCs were collected at each time point.

B. Illustration of a single step of the iGraphBoost procedure to classify RGCs collected at time t_{n+1} based on an atlas of RGC types at the previous time point t_n. The procedure is initiated with Atlas RGCs at t_0. In **Step 1**, gradient boosted trees trained on t_n RGC types are used to classify t_{n+1} RGCs. Only high-confidence assignments are applied, and a large number of RGCs remain unclassified at this stage. In **Step 2**, a Jaccard-weighted k-nearest neighbor graph built on all t_{n+1} RGCs is used to propagate labels via nearest-neighbor voting to unassigned RGCs, using the classified RGCs in step 1 as anchors. Successfully classified t_{n+1} RGCs are used to classify t_{n+2} RGCs in the next iteration.

C. Fraction of RGCs that can be confidently assigned to types (y-axis) at each time point following ONC (x-axis). The "one-step" approach (grey) using the atlas RGCs as training

data results in a significantly lower proportion of assigned cells among late injured RGCs compared to iGraphBoost (black).

D. Dotplot showing that gene combinations uniquely defining each RGC type (row and column order as in Figure 1F) are maintained in 14dpc assigned by iGraphBoost, though reduction in expression level of some markers was observed.

E. RGC type-specific resilience at 14dpc relative to control (Ctrl) rank ordered based on decreasing values of the relative frequency ratio at 14dpc vs. Ctrl. RGC types exhibit a wide spectrum of survival at 14dpc ranging from 1–98%.

F. 14d survival ranking (as in E) colored by RGC subclasses. Overlapping subclasses are denoted by two-tone color bars.

G. 14d survival ranking (as in E) colored by relative abundance in control.

H. Scatter plot showing correspondence between the 14dpc survival rates of RGC groups as determined by scRNAseq and IHC ($R_{Pearson}$ =0.97). 26 combinations of antibodies and transgenic lines (Table S3) were used label groups of RGC types covering a broad frequency range.

I. Loss of RGC somas as determined by IHC for RBPMS in this study (diamonds; see Figure S4F for example images) or by retrograde labeling from superior colliculus (triangles; redrawn from (Galindo-Romero et al., 2011)).

J. -M. Each RGC type can be assigned to one of three survival groups based on the pattern of cell loss across time. Individual graphs of relative survival, defined as the fraction of cells surviving at each time point, shown for 7 resilient types (J), 11 intermediate types (K) and 27 susceptible types (L), (see also S3G). Fluctuations in sampling frequency resulted in relative survival values >1 through 2dpc (where there is little death) for rare RGC types (frequency < 0.5%). Error bars are not included for individual types in panel **K-L** for clarity of presentation. Grey lines, relative survival for each type within the survival group; colored lines, mean relative survival across types; shaded ribbons, standard deviation of relative survival values across types. Fluctuations observed through 2dpc were within expected error (colored ribbons), in contrast to later time points. Solid lines, mean relative survival across types within a survival group; shaded ribbons, standard deviation. Group means are superimposed in **M**.

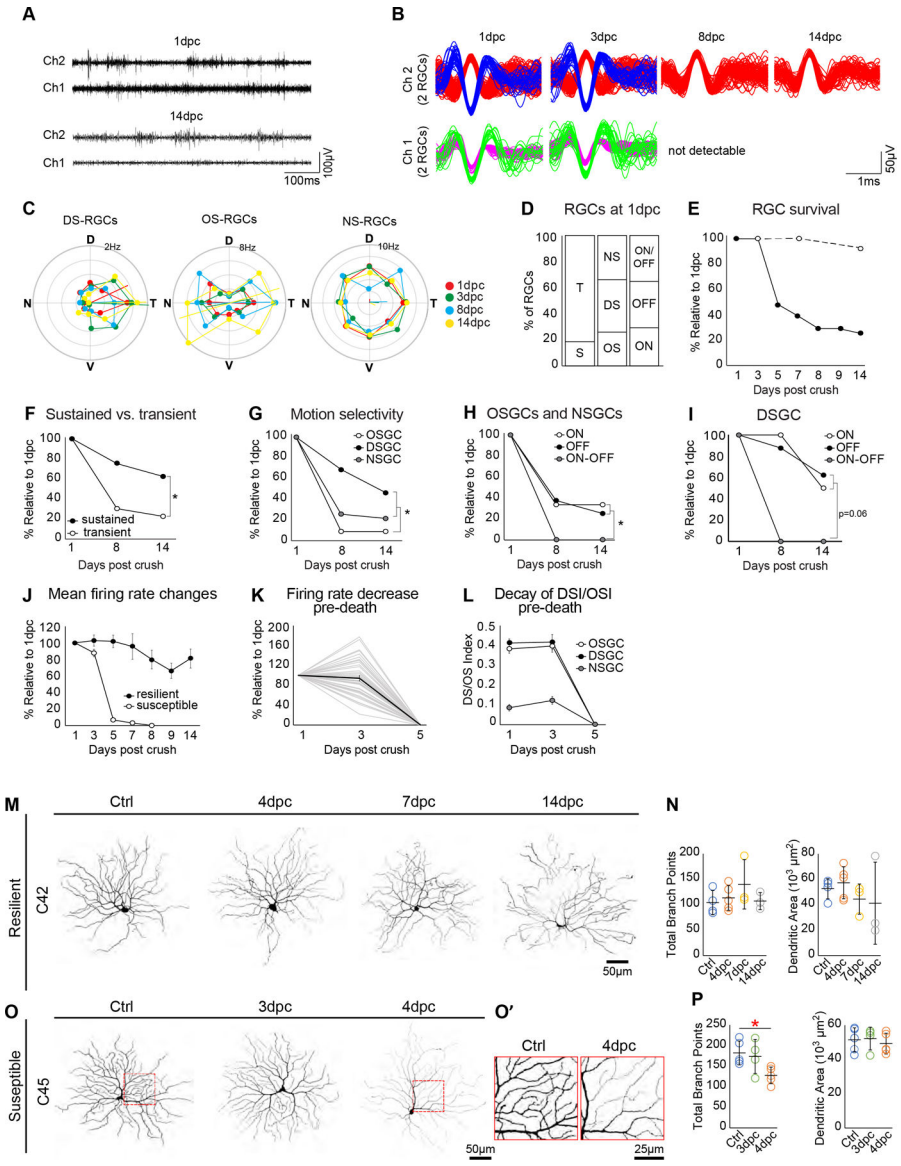

Figure 4. Physiological characteristics of resilient and susceptible RGCs

A. Representative recordings of two out of 32 channels in 1dpc and 14dpc mesh-implanted retinas.

B. Sorted spike waveforms for two individual RGCs per channel (rows) represented in **A** recorded over multiple days. Ch1 shows spike waveforms of two sorted RGCs (purple and green lines) on 1dpc and 3dpc; cells have died by 8dpc. Ch2 shows waveforms of two sorted RGCs (blue and red) on 1dpc and 3dpc, but only one RGC was still detectable at 8dpc.

C. Polar plots of responses of direction-selective (DS), orientation-selective (OS) and neither orientation- nor directions-selective (NS) RGCs to gratings moving in each of 8 directions. Each plot shows measurements from the same cell on different days.

D. Proportion of RGCs by response type within each response category (columns) at 1dpc. S, sustained, T, transient, ON, OFF and ON/OFF, responds to light increments, decrements or both.

E. RGC survival as a function of time in physiological recordings following ONC (black line) compared to uncrushed control (dotted line shows data replotted from (Hong et al., 2018))

F. Sustained RGCs survive better than transient RGCs as assessed by physiology (* = $p<0.03$ by Fisher's Exact Test).

G. OSGCs are more susceptible than DSGCs or NSGCs (* = $p<0.04$ by Fisher's Exact Test).

H. Among RGCs that are either OS or NS, ON-OFF cells are more susceptible than ON or OFF cells (* = $p<0.03$ by Fisher's Exact Test).

I. Among DSGCs, ON-OFF cells (ooDSGCs) are susceptible than ON or OFF cells ($p=0.06$ at 14dpc by Fisher's Exact Test).

J. Average firing rates for RGCs that survive until 14dpc or die by 8dpc.

K. RGCs that are dead by 5dpc exhibit little changes in firing rate between 1–3dpc.

L. RGCs that are dead by 5dpc exhibit little change in direction/orientation selectivity index (DSI/OSI) between 1–3dpc.

M. *En face* morphology of resilient RGCs (αOFF-S, C42) at Ctrl, 4, 7, and 14dpc.

N. Quantification of C42 morphological complexity (total branch points) and size (dendritic area) shows no significant difference between time points for either measure (one-way ANOVA with post-hoc Tukey HSD test). Data are shown as mean±SD.

O. *En face* morphology of susceptible RGCs (αOFF-T, C45) at Ctrl, 3, and 4dpc. O' showing zoomed in views of dendrites at Ctrl and 4dpc.

P. Quantification of C45 morphological complexity as in N. * = $p<0.04$; one-way ANOVA with post-hoc Tukey HSD test. Data are shown as mean ±SD.

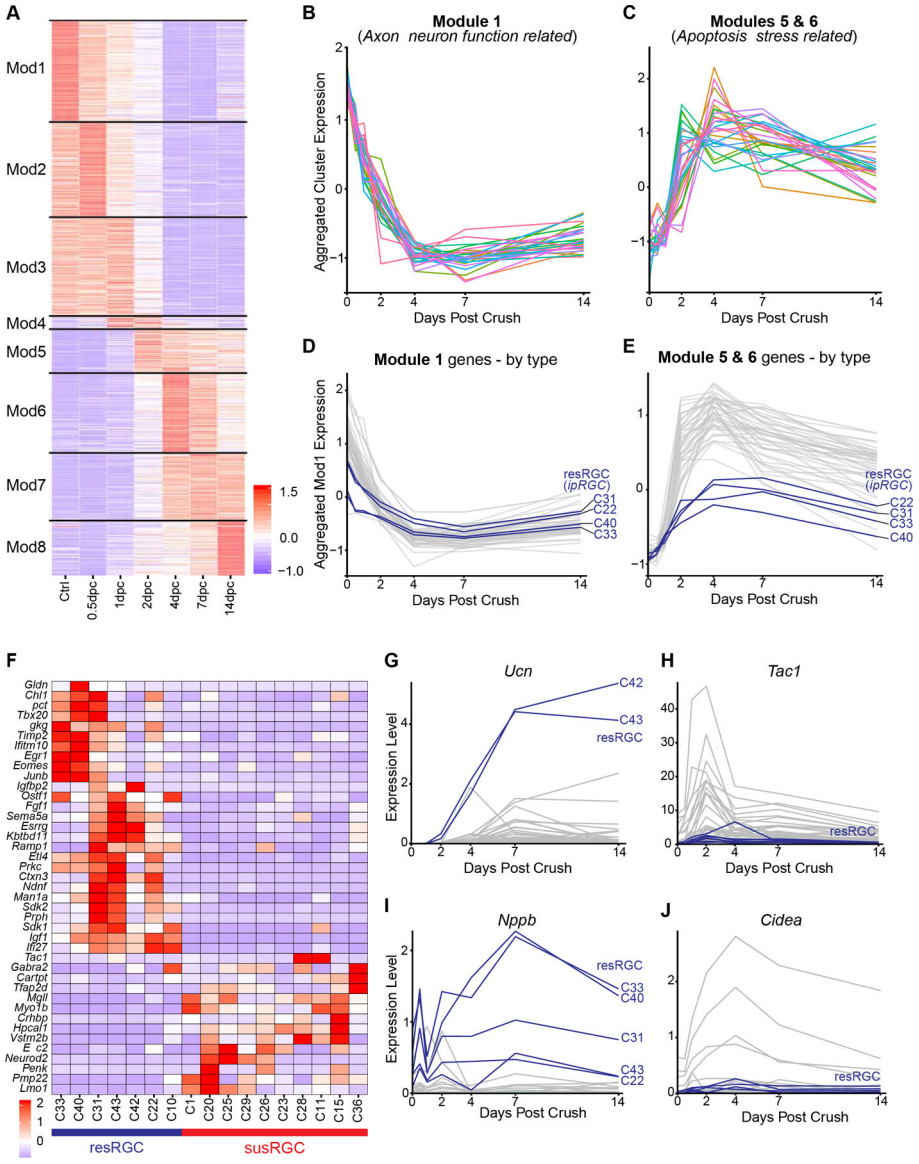

Figure 5. Global changes in gene expression following injury

A. Heatmap of genes showing temporal variation following ONC. Expression values of each gene (row) is averaged across all RGCs at a given time point (columns), and then z-scored across times prior to plotting. Black bars separate genes into 8 modules (Mod) based on temporal dynamics.

B. Mean temporal dynamics of individual genes (lines) from Module 1 that were associated with gene ontology (GO) biological processes related to axon and neuronal functions. Genes and the GO processes from which they were selected are listed in Table S4.

C. As in **B**, for Modules 5 and 6 for genes associated GO biological processes related to apoptosis or various stress pathways.

D. Expression dynamics of genes from B plotted for each RGC type (lines). Blue lines correspond to ipRGC types (C31, 22, 40, 33). Expression values for each type were z-scored to track relative changes.

E. Same as **D**, for genes from **C**

F. Expression patterns of DE genes (rows) distinguishing the 7 resRGC types and the 10 most susceptible RGC types (columns), based on 14dpc survival in the uninjured retina (Figure 3F). Values were z-scored along each row prior to plotting.

G. -J. Averaged temporal dynamics of candidate genes selectively upregulated in resRGC or susRGC types (lines). Blue lines correspond the 7 resRGC types, including types that upregulate *Ucn* (C42, 43) or *Nppb* (C22, 31, 33, 40, 43) (left panels), which were not enriched for *Tac1* or *Cidea* (right panels).

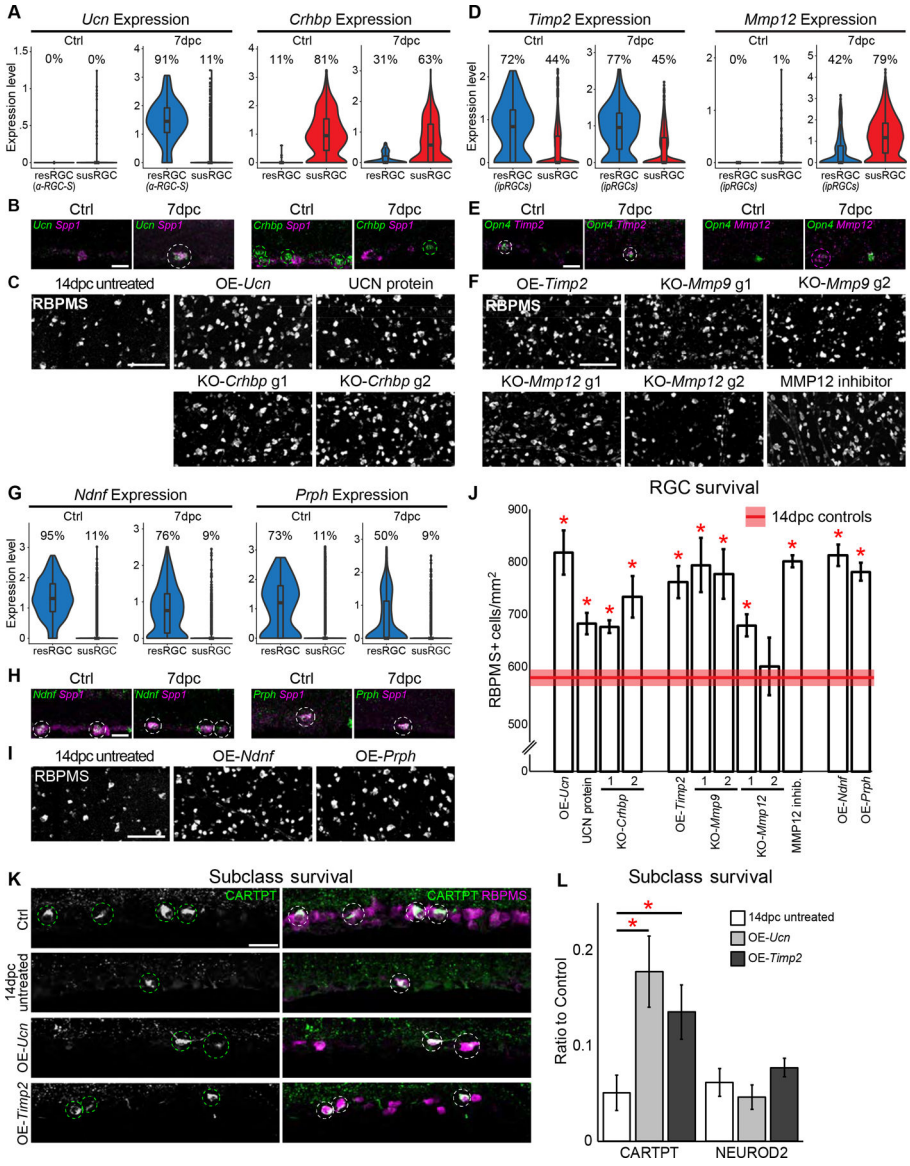

Figure 6. Genes that affect RGC survival

A. *Ucn* is selectively upregulated in sustained αRGC's (α-RGC-S; C42, 43) and *Crhbp* is selectively expressed in a subset of susRGC types (C14, 15, 17, 24, 26, 28, 39). Violin plots show merged expression for indicated clusters at 0 and 7dpc. The number above the violins indicates the percentage of cells expressing the marker within each subset. Box plots depict the median and interquartile range.

B. FISH of retinal sections shows *Ucn* upregulation at 7dpc in *Spp1*+ RGCs (α-RGCs marker): white circles. *Crhbp* is expressed in a set of *Spp1*- RGCs (non-α-RGCs) before and after ONC: green circles.

C. IHC in retinal whole mounts for RBPMS shows increased survival of RGCs at 14dpc following OE-*Ucn*, KO-*Crhbp*, or injection of UCN protein.

D. *Timp2* is selectively expressed in the resilient ipRGCs (C22, 31, 33, 40, 43) before and after ONC. *Mmp12* is upregulated in a broad subset of susRGCs (C7, 8, 11, 12, 14, 17, 18,

23, 24, 27, 28, 43, 37, 39, 41) after crush but is low in ipRGCs in scRNAseq data. Violin plots as in **A**.

E. FISH of retinal sections as in **B**.

F. IHC in retinal whole mounts as in **C**.

G. Expression in resRGC subsets at 0 and 7dpc of *Ndnf* (C22, 31, 43) and *Prph* (C31, 43). Violin plots as in panel **A**.

H. FISH of retinal sections as in **B**.

I. IHC of retinal whole mounts as in **C**.

J. Total RGC survival (RBPMS+ cells; mean ± SEM) in whole mounts following interventions shown in **C**, **F**, and **I**. Red line and ribbon, mean RBPMS density ±SEM averaged from four sets of controls, which did not differ significantly from each other: no injection, PBS, UCN vehicle, and MMP12 inhibitor vehicle. n=18; details in STAR methods. *adjusted p-value <.05 (Bonferroni).

K. IHC showing increased survival of CARTPT+ RGCs (circles) at 14dpc following OE-*Ucn* and OE-*Timp2* compared to vehicle. Top row, $CARTPT^{+}$ RGCs at 0dpc.

L. IHC quantification showing selective survival of $CARTPT^{+}$ RGCs (C12, 14, 16, 36) compared to $NEUROD2^{+}$ RGCs (C12, 19, 20, 25, 26, 29, 35, 39) at 14dpc following indicated treatments. y-axis, #positive per section RGCs at 14dpc/control. Performed on retinal sagittal sections through the optic nerve. * p-value <.05 (FDR adjusted).

Scale bar: 25μm for **B,D,H,K**; 100μm for **C,F,I**

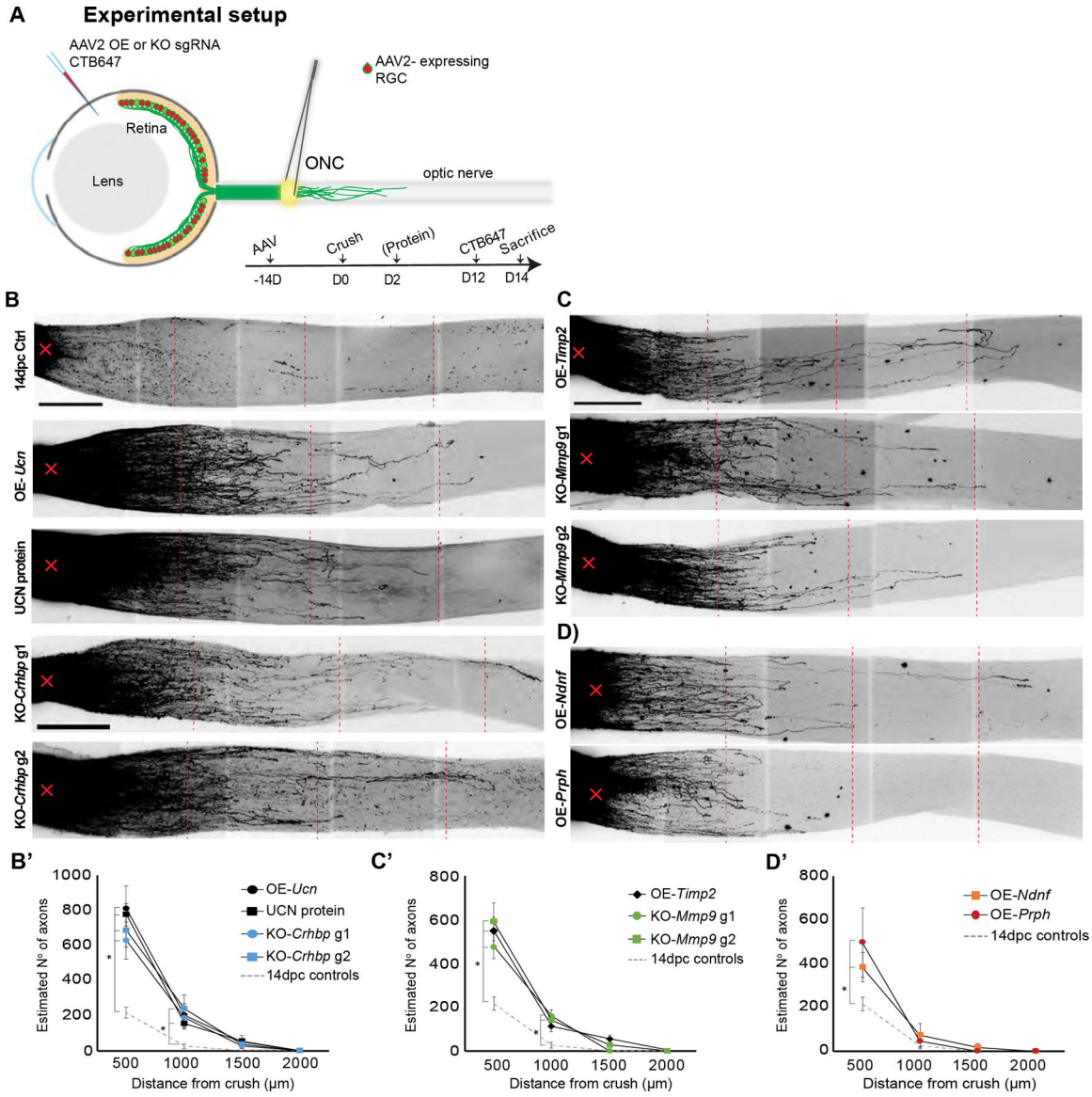

Figure 7. Genes that promote RGC axon regeneration

A. *In vivo* OE and KO. An AAV2 carrying the OE gene or KO sgRNA is injected intravitreally 14 days before the crush. At 12dpc regenerating axons are anterogradely labeled via CTB647 injection. UCN protein was injected at 2dpc.

B. Maximum projections of cleared optic nerves showing anterograde-labeled RGC axons at 14dpc following vehicle injection or indicated treatment of Ucn (OE or protein) and KO-*Crhbp* (g1 and g2).

C. Same as **B**, following OE-*Timp2* and KO-*Mmp9* (g1 and g2).

D. Same as **B**, following OE-*Ndnf* and OE-*Prph*.

E. -G. Quantification of axon regeneration. Control line represents mean±SEM from three groups, which did not differ significantly from each other: PBS only, UCN vehicle and AAV-Cre with no sgRNA; n=14; details in STAR methods. * $p < 0.05$ two-tailed Student's t-test

of area under the curve evaluated using numerical integration. Mixed effects analysis with Bonferroni correction for individual distances are shown in Table S6.

In **B-D**, Scale bar, 250μm; X = crush site; red lines - 500, 1000, 1500μm distances from crush site.

KEY RESOURCES TABLE

REAGENT or RESOURCE	SOURCE	IDENTIFIER
Antibodies		
Mouse monoclonal anti-Brn3c (Pou4f3)	Santa Cruz	Cat#sc-81980;RRID:AB_2167543
Rabbit polyclonal anti-Calbindin	Swant	Cat#CB-38a
Rabbit polyclonal anti-Calretinin	Millipore	Cat#AB5054;RRID:AB_2068506
Goat polyclonal anti-Chat	Millipore	Cat#AB144P;RRID:AB_2079751
Goat polyclonal anti-Foxp2	Abcam	Cat#ab1307;RRID:AB_1268914
Chicken polyclonal anti-GFP	Abcam	Cat#ab13970;RRID:AB_300798
Rabbit polyclonal anti-DsRed	Takara	Cat#632496;RRID:AB_10013483
Mouse monoclonal anti-Mmp12	Santa Cruz	Cat#sc-390863
Rabbit polyclonal anti-Mmp9	Abcam	Cat#ab38898;RRID:AB_776512
Rabbit polyclonal anti-Neurod2	Abcam	Cat#Ab104430;RRID:AB_10975628
Rabbit polyclonal anti-Opn4	Thermo Scientific	Cat#PA1–780;RRID:AB_2267547
Guinea pig polyclonal anti-Prdm8	Kind gift from Sarah E. Ross lab	Ross et al., 2012
Guinea pig polyclonal anti-Rbpms	PhosphoSolutions	Cat#1832-RBPMS;RRID:AB_2492226
Rabbit polyclonal anti-Rbpms	Abcam	Cat#ab194213
Rabbit polyclonal anti-Satb1	Epitomics	Cat#2938–1;RRID:AB_2184447
Mouse monoclonal anti-Satb2	Abcam	Cat#Ab51502;RRID:AB_882455
Mouse monoclonal anti-SMI32	Covance	Cat#SMI-32P;RRID:AB_2314912
Goat polyclonal anti- Spp1 (Osteopontin)	R&D Systems	Cat#AF808;RRID:AB_2194992
Rabbit polyclonal anti-Tbr2 (Eomes)	Abcam	Cat#Ab183991;RRID:AB_2721040
Rabbit polyclonal anti-Tbx20	Boster Bio (discontinued)	Cat#A04704
Rabbit polyclonal anti-Urocortin (Ucn)	Sigma Aldrich	Cat#SAB4300830
Goat polyclonal anti-Vacht	Progema (discontinued)	Cat#G4481;RRID:AB_430859
Chemicals, Peptides, and Recombinant Proteins		
Alexa-conjugated cholera toxin subunit B (CTB647)	Thermo Fisher	Cat#C34778
AMES' Medium	Sigma	Cat#A1420
Papain	Worthington	Cat#LS003126
Ovomucoid	Worthington	Cat#130042202
Fluoromount-G	Southern Biotech	Cat#0100–20
Visikol® HISTO-1™ and Visikol® HISTO-2™ Combo	Visikol	Cat#HH10
Anti-Fluorescin-POD, Fab fragments	Roche	Cat#11426346910
Anti-Digoxigenin-POD, Fab fragments	Roche	Cat#11207733910
Anti-DNP-HRP	Perkin Elmer	Cat#FP1129
TSA Cyanine 3 Plus Evaluation Kit	Perkin Elmer	Cat#NEL744E001KT (FP1170)
TSA Cyanine 5 Plus Evaluation Kit	Perkin Elmer	Cat#NEL745E001KT (FP1171)
TSA Fluorescein Plus Evaluation Kit	Perkin Elmer	Cat#NEL741E001KT (FP1168)
ActinomycinD	Sigma-Aldrich	Cat#A1410

REAGENT or RESOURCE	SOURCE	IDENTIFIER
Poly-D-lysine	Sigma-Aldrich	Cat#P6407
Urocortin (rat) small peptide	Millipore Sigma	Cat#U6631
Mmp12 Inhibitor	Millipore Sigma	Cat#444291
Critical Commercial Assays		
Chromium Single Cell 3'Library & Gel Bead Kit v2, 16rxns	10X Genomics	Cat#120237
Chromium Single Cell A Chip Kit, 16rxns	10X Genomics	Cat#1000009
Chromium i7 Multiplex Kit 96 rxns	10X Genomics	Cat#120262
TruSeq Total RNA	Illumina	
RNAscope Fluorescent Multiplex Reagent Kit	Advanced Cell Diagnostics	Cat#320850
RNAscope® Probe Diluent	Advanced Cell Diagnostics	Cat#300041
Deposited Data		
Raw data files for RNA-sequencing	This manuscript	GEO: https://singlecell.broadinstitute.org/single_cell/study/SCP509/mouse-retinal-ganglion-cell-adult-atlas-and-optic-nerve-crush-time-series
Experimental Models: Organisms/Strains		
Mouse: C57Bl/6	Charles River or Jackson Labs	Cat#JAX000664;RRID:IMSR_JAX:000664
Mouse: Slc17a6$^{tm2(cre)Lowl}$/J	Jackson Labs	Cat#JAX016963;RRID:IMSR_JAX:016963
Mouse: B6.Cg-Tg(Thy1-EYFP)15Jrs/J	Joshua Sanes (Buffelli et al., 2003)	Cat#JAX005630;RRID:IMSR_JAX:005630
Mouse: B6.Cg-Tg(Thy1-YFP)W3Jrs/J	Joshua Sanes (Kim et al., 2010)	Cat#JAX033114;RRID:IMSR_JAX:033114
Mouse: B6.129(SJL)-Kcng4$^{tm1.1(cre)Jrs/J}$	Joshua Sanes (Duan et al., 2014)	Cat#JAX029414;RRID:IMSR_JAX:029414
Mouse: T*hy1-stop-YFP Line#1*	Joshua Sanes (Buffelli et al., 2003)	N/A
Mouse: Tg(Jam2-cre/ERT2)2Jrs/J	Joshua Sanes (Kim et al. 2008)	Cat#JAX029417;RRID:IMSR_JAX:029417
Mouse: *Cck*$^{tm1.1(cre)Zjh}$/J	Jackson Labs	Cat#JAX012706;RRID:IMSR_JAX:012706
Mouse: B6.129P2-*Pvalb*$^{tm1(cre)Arbr}$/J	Jackson Labs	Cat#JAX017320;RRID:IMSR_JAX:017320
Mouse: Opn4-Cre	Ecker et al. 2010	N/A
Mouse:Rosa-lox-STOP-lox-Tomato	Zhigang He (Madisen et al., 2010)	N/A
Mouse: B6;129-*Gt(ROSA)26Sor*$^{tm1(CAG-cas9*,-EGFP)Fezh}$/J	Jackson Labs	Cat#JAX024857;RRID:IMSR_JAX:024857
Mouse: B6.Cg-Tg(Thy1-YFP)HJrs/J	Joshua Sanes (Feng et al., 2000)	Cat#JAX003782;RRID:IMSR_JAX:003782
Mouse: B6.Cg-Tg(Hlxb9-GFP)1Tmj/J	Joshua Sanes (Trenholm et al., 2011)	Cat#JAX005029;RRID:IMSR_JAX:005029
Mouse: TYW7 (Thy1-lox-YFP-STOP-lox_WGA-ires-LacZ)	Joshua Sanes (Kim et al. 2010)	N/A
Mouse: B6;129S-*Penk*$^{tm2(cre)Hze}$/J	Jackson Labs	Cat#JAX025112;RRID:IMSR_JAX:025112
Oligonucleotides		
Primer used to generate ISH probes	IDT	Table S8
RNAScope probes	A.D.T.	Table S8

REAGENT or RESOURCE	SOURCE	IDENTIFIER
Primer for overexpression cloning	IDT	Table S8
Primer for sgRNA cloning	IDT	Table S8
Recombinant DNA		
pAAV2-hSyn-hChR2(H134R)-EYFP	Gift from Karl Deisseroth	Addgene plasmid Cat#26793; RRID:Addgene_26973
AAV-U6-sgRNA-hSyn-mCherry	Gift from Alex Hewitt	Addgene plasmid Cat#87916; RRID: Addgene_87916
pAAV2-hSyn-Ucn-WPRE	BCH Viral Core	N/A
pAAV2-hSyn-Timp2-WPRE	BCH Viral Core	N/A
pAAV2-hSyn-Ndnf-WPRE	BCH Viral Core	N/A
pAAV2-hSyn-Prph-WPRE	BCH Viral Core	N/A
pAAV2-U6-Crhbp g1-hSyn-mCherry	BCH Viral Core	N/A
pAAV2-U6-Crhbp g2-hSyn-mCherry	BCH Viral Core	N/A
pAAV2-U6-Mmp12 g1-hSyn-mCherry	BCH Viral Core	N/A
pAAV2-U6-Mmp12 g2-hSyn-mCherry	BCH Viral Core	N/A
pAAV2-U6-Mmp9 g1-hSyn-mCherry	BCH Viral Core	N/A
pAAV2-U6-Mmp9 g2-hSyn-mCherry	BCH Viral Core	N/A
pAAV2-U6-Tac1 g1-hSyn-mCherry	BCH Viral Core	N/A
pAAV2-U6-Tac1 g2-hSyn-mCherry	BCH Viral Core	N/A
pAAV2-U6-Hpcal1 g1-hSyn-mCherry	BCH Viral Core	N/A
pAAV2-U6-Hpcal1 g2-hSyn-mCherry	BCH Viral Core	N/A
pAAV2-U6-Evc2 g1-hSyn-mCherry	BCH Viral Core	N/A
pAAV2-U6-Evc2 g2-hSyn-mCherry	BCH Viral Core	N/A
pAAV2-CAG-Cre-WPRE-hGH	BCH Viral Core	Belin et al., 2015
Software and Algorithms		
ImageJ (Fiji)	Schindelin et al., 2012	https://imagej.net/Fiji
SNT	Longair et al., 2011	https://imagej.net/Simple_Neurite_Tracer
Cell Profiler	Carpenter et al., 2006	https://cellprofiler.org
Prism 8.0	GraphPad Software	https://www.graphpad.com/
SPSS	IBM Corp. Released 2017. IBM SPSS Statistics for Windows, Version 25.0. Armonk, NY: IBM Corp.	https://www.ibm.com/products/spss-statistics
StringTie v1.3.3	Pertea et al., 2016	https://ccb.jhu.edu/software/stringtie/
Cell Ranger v2.1.0	10X Genomics	https://support.10xgenomics.com/single-cell-gene-expression/software/downloads/latest
Hisat2	Kim et al., 2019	https://ccb.jhu.edu/software/hisat2/index.shtml
R for statistical computing version 3.6.0	N/A	https://cran.r-project.org/
Bioconductor software packages	Gentleman et al.,2004	http://bioconductor.org/
Mathworks	custom written codes	https://www.mathworks.com/
Custom R scripts	This manuscript	https://github.com/klarman-cell-observatory/RetinalGanglionCell-ONC
Other		

REAGENT or RESOURCE	SOURCE	IDENTIFIER
LSM 710 scanning confocal microscope	Zeiss	N/A
Olympus FV-1000 confocal microscope	Olympus	N/A
HiSeq 2500 System	Illumina	N/A
NextSeq 500 System	Illumina	N/A
Chromium controller	10x Genomics	N/A
Mesh electronics	(Hong et al., 2018)	N/A